The University Of Sheffield.

This is a repository copy of *Twin nucleation and variant selection in Mg alloys: An integrated crystal plasticity modelling and experimental approach*.

White Rose Research Online URL for this paper:
https://eprints.whiterose.ac.uk/171770/

Version: Accepted Version

Article:

White Rose
university consortium
Universities of Leeds, Sheffield & York

eprints@whiterose.ac.uk
https://eprints.whiterose.ac.uk/

Twin nucleation and variant selection in Mg alloy: an integrated crystal plasticity modelling and experimental approach

Chaitanya Paramatmuni [a], Zebang Zheng [c], W. Mark Rainforth [b], Fionn PE Dunne [a]

a. Department of Materials, Imperial College London, London SW7 2AZ, United Kingdom
b. Department of Materials Science and Engineering, University of Sheffield, Sheffield S1 3JD, United Kingdom
c. School of Materials Science and Engineering, Northwestern Polytechnical University, China

Abstract

Extension twin nucleation and variant selection in magnesium alloy WE43 is investigated in experimentally characterised and deformed microstructures replicated in crystal plasticity models. Stored (dislocation) energy density is found to identify the experimentally observed locations of twins which are not otherwise explained by global Schmid factors or local resolved shear stress criteria. A critical stored energy of 0.015 Jm^{-2} was determined below which twin nucleation does not occur. The stored energy density explains the locations of the observed twins and the absence of twins in parent grains anticipated to be favourable for twin nucleation. Twin variant selection has been shown to be driven by minimising locally stored shear energy density, while the geometric compatibility and strain compatibility factors only aid in partial prediction. All experimentally observed variants were correctly determined.

Keywords: HCP; Twin nucleation; Rare-earth alloy; Stored energy density; Variant selection; Crystal plasticity.

1. Introduction

There is increasing interest in light metals in automobile industries and good strength to weight ratio makes Magnesium (Mg) alloy one of the candidate materials [Joost and Krajewski (2017)]. However, Magnesium and its alloys are limited by their poor formability and ductility due to the hexagonal close-packed (HCP) crystallographic anisotropy. Mg alloys commonly exhibit strong 'basal' texture with the basal poles aligned with the sheet normal direction after rolling [Styczynski et al. (2004), Mackenzie and Pekguleryuz (2008)]. Such texture results in modest work hardening and non-uniform elongation during deformation. It has been reported that the addition of rare earth (RE) elements, e.g. Cerium (Ce), Neodymium (Nd) and Yttrium (Y), can modify the conventional rolling texture [Bohlen et al. (2007), Hantzsche et al. (2010), Hadorn et al. (2013), Imandoust et al. (2017)]. Typical Mg-RE alloys exhibit a weak basal texture with the basal pole tilted towards the normal direction and transverse direction after rolling and/or annealing [Al-Samman and Li (2011), Guan et al. (2017a)]. The formability of Mg alloys can thus be improved by achieving a RE-texture which reduces the anisotropy.

At low temperatures, basal slip in Mg is activated at lower shear stress than prismatic or pyramidal systems, making ⟨a⟩-basal slip the preferred slip mode [Partridge (1967)]. Due to the limited number of easy slip systems in Mg alloys, deformation twinning that can accommodate strain along the crystal c-direction provides an alternative mode of plastic deformation. Twinning occurs by the formation of a nucleus which then propagates along the twin direction on the corresponding twin plane, where it continuously shears and reorients the parent grain [Christian and Mahajan (1995)]. It is therefore essential to understand the twinning mechanism to enable control over the microstructure and texture evolution.

The commonly observed twin mode in Mg alloys is the $\{10\bar{1}2\}[\bar{1}011]$ extension twin [Partridge (1967), El Kadiri et al. (2015)]. Due to the symmetry of the HCP crystal structure, there are six possible extension twin variants in Mg. Extensive work has been carried out to

25 establish the mechanistic basis of twin nucleation and variant selection. The most widely

26 reported criterion is based on global Schmid factor that assumes a stress state resulting from

27 remote loading conditions. Jonas et al. (2011) have shown that only half of activated twins have

28 the highest global Schmid factors (e.g. >0.3). Similarly, statistical analysis of twin nucleation

29 and corresponding microstructural features in Mg [Beyerlein et al. (2010)] and Zr [Capolungo

30 et al. (2009)] show that 47%~60% of twins have the highest global Schmid factors on the

31 activated variant, while the 21%~27% have the second highest. It is suggested that the local

32 stress variation is responsible for the activation of twin variants with smaller global Schmid

33 factors, although the local resolved shear stress has not been investigated quantitatively (see

34 also [Livescu et al. (2019)]. In many modelling approaches, critical resolved shear stress

35 (CRSS) is typically used to describe twin formation [Proust et al. (2009), Wang et al. (2013),

36 Wu et al. (2015)]. A probabilistic twin nucleation model has been proposed by Beyerlein and

37 Tomé (2010) which assumes a Poisson distribution of threshold shear stress to predict twin

38 nucleation. This model was incorporated within crystal plasticity-phase field modelling [Liu

39 et al. (2018)] to study the spatial twin formation process. However, experimental observations

40 suggest that global Schmid factors calculated from macroscopic loading cannot fully explain

41 the observed twins [Molodov et al. (2016), McClelland et al. (2015), Sevillano (2008), Livescu

42 et al. (2019)]. This indicates that the twins are not always driven by stress alone. Gradients in

43 plasticity established within parent grains can be mitigated by twin nucleation to achieve strain

44 accommodation [McClelland et al. (2015)]. In the cases where twin nucleation is not stress

45 driven, low/negative Schmid factors (non-Schmid) have been observed [Molodov et al.

46 (2016)]. The negative Schmid factors may also result in negative local resolved shear stress

47 associated with the observed active twin variant in the microstructure.

48 The non-Schmid twin variant selection is typically explained using the geometric compatibility

49 factor and the shear strain accommodations. Both direct and indirect slip transmission may

occur at grain boundaries. Various models including the N factor [Livingston and Chalmers

(1957)], the geometric compatibility factor (m') [Luster and Morris (1995)], and the residual

burgers vector method (e.g. [Lim and Raj (1985)] have been utilised to investigate slip transfer.

Of these three factors, the geometric compatibility factor (m′) has been extensively used as it

shows better predictions [Bieler et al. (2014), Guo et al. (2015)], and is based on the degree of

coplanarity of incoming and outgoing slip systems across the grain boundary. It was later

extended to investigate twin variant selection and twin-assisted-twinning in HCP materials

[Wang et al. (2010), Xin et al. (2015), Guo et al. (2014), Nervo et al. (2016), Kumar et al.

(2016)]. In addition, the selection of non-Schmid variants by the parent grain has also been

investigated by studying the shear strain accommodations that are required in the neighbouring

grain to permit twin variant formation [Jonas et al. (2011)]. It has been shown that the twin

variant which requires least strain accommodation by prismatic slip and the highest by basal

slip is selected by the parent grain.

Energy based criteria have also been employed to study twin formation. For instance, Wang

et al. (2012) proposed a deformation energy criterion for twin variant selection. The correct

prediction of variant selection increased from 50% using a global Schmid factor criterion to

80% using the energy criterion. The crystal plasticity finite element (CPFE) modelling work

by Cheng et al. [Cheng and Ghosh (2015), Cheng and Ghosh (2017)] also uses an energetic

criterion, where twin nucleation occurs when the initial energy of $\langle c + a \rangle$ dislocations

generated in the parent grain exceeds the energy of $\langle c + a \rangle$ dislocation dissociation event.

Similarly, the energetic twin nucleation model introduced by Capolungo and Beyerlein (2008)

is based on the dissociation of $\langle a \rangle$ type dislocations. From these studies it is evident that the

energy arising from slip to maintain the local dislocation structure may lead to twin nucleation.

In this context the local stored energy density, which is based on evolution of dislocation

74 structure, and which has been shown to be a driver for fatigue crack nucleation in materials

75 [Wan et al. (2014), Chen et al. (2018)], may also be a useful approach.

76 Twin nucleation and variant selection are complex phenomena requiring knowledge of

77 macroscopic loading, material properties, microstructure and the local stress and stored energy

78 variations. In this paper, we utilise a systematic methodology which integrates a physically

79 based crystal plasticity model and experiments aiming to establish new understanding of both

80 twin nucleation and variant selection in WE43 alloy. In the next section, the experimental

81 procedure and crystal plasticity approach are briefly outlined. Results are then presented,

82 assessing twin nucleation and variant selection from the experimental observations, together

83 with material property determination and comparison of the results with the CPFE analysis of

84 twin nucleation. Finally, we investigate twin variant selection utilising both the experimental

85 observations and CPFE calculations based on local stored energy. This is followed by

86 discussion and conclusions.

87 **2. Methodology**

88 **2.1 Experimental procedure**

89 Mg alloy WE43 was received as an extruded bar supplied by Magnesium Elektron with the

90 composition and texture shown in Guan et al. (2017b). Compression samples with dimensions

91 of 4×4×8 mm (ASTM E9-09) were cut to calibrate the constitutive model and to investigate

92 twin nucleation. The compression was performed along the transverse direction (TD) until ~5%

93 strain in a Zwick/Roell™ 100 kN machine at room temperature at a strain rate of 0.1 s^{-1}.

94 Electron backscattered diffraction (EBSD) was performed on the sample before and after

95 deformation in ZEISS Sigma 300™ SEM equipped with Bruker high resolution EBSD detector

96 with voltage of 20 kV and ~13 mm working distance. The sample was mechanically polished

97 until 4000 grit silicon carbide papers followed by fine polishing using 50 nm colloidal silica

98 suspension for about 30 minutes. The sample was then Ar ion polished with a PECS-II system

99   under dual beam condition using 4.0 keV beam energy with rotational speed of 4 rpm for about

100   40 minutes, followed by 20 minutes fine polishing using 2.0 keV and a speed of 2 rpm. A large

101   area of 831×505 μm^2 was scanned with step size of 3 μm to obtain the undeformed

102   microstructure. After deformation, a sub-region of interest of area 159×122 μm^2 from this large

103   area was further scanned for high resolution electron backscattered diffraction (HR-EBSD)

104   analysis with a step size of 0.3 μm. The Kikuchi patterns with binning of 2×2 were saved for

105   offline digital image cross-correlation.

2.2. Constitutive framework

107   The strain gradient and rate dependent crystal plasticity finite element formulation developed

108   in Dunne et al. (2007) is utilized to study twin nucleation. A brief description of the formulation

109   is presented here. The total deformation gradient $\mathbf{F}$ is decomposed into elastic ($\mathbf{F^e}$) and plastic

110   deformation gradient tensors ($\mathbf{F^p}$) as

$$\mathbf{F} = \mathbf{F^e}\mathbf{F^p} \tag{1}$$

111   The plastic velocity gradient considers the contributions from all slip systems and is expressed

112   as

$$\mathbf{L^p} = \sum_i \dot{\gamma}^i \mathbf{n}^i \otimes \mathbf{s}^i \tag{2}$$

113   where $\mathbf{n}^i$ and $\mathbf{s}^i$ are the plane normal and direction of slip system i respectively. The slip rate

114   considering both forward and backward thermally activated dislocations escape is given by

$$\dot{\gamma}^i = \rho_m b^{i^2} \nu_D \exp\left(-\frac{\Delta F}{kT}\right) \sinh\left(\frac{(\tau^i - \tau_c^i)\Delta V^i}{kT}\right) \tag{3}$$

115   in which ρ_m is the mobile dislocation density, b^i the Burgers vector magnitude, ν_D the Debye

116   frequency, k the Boltzmann constant, T the temperature, τ^i and τ_c^i are the resolved shear stress

117 (RSS) and the corresponding critical resolved shear stress (CRSS) for slip system i. The strain

118 rate sensitivity is determined by an activation energy ΔF and a corresponding activation volume

119 ΔV^i for slip system i. The hardening law is given by the evolution of the CRSS based on the

120 development of dislocation density as

$$\tau_c^i = \tau_{c0}^i + \alpha G b^i \sqrt{\rho_{SSD} + \sum_{i=1}^{n} \rho_{GND}^i} \tag{4}$$

121 where τ_{c0}^i is the initial slip resistance on the slip system, α the hardening coefficient and G the

122 shear modulus. ρ_{SSD} and ρ_{GND} are the density of statistically stored (SSD) and geometrically

123 necessary dislocations (GND) respectively. The SSD density is evolved as a function of plastic

124 strain rate $\dot{p}$ at a material point as

$$\rho_{SSD} = \int_0^t \gamma' \dot{p} \, dt \tag{5}$$

125 where γ' determines the rate of density evolution. The distribution of GND density is calculated

126 from strain gradients accommodating lattice curvatures. Further details of the GND calculation

127 can be found in Dunne et al. (2012). In summary, the Nye tensor is related to the GND density

128 on an individual slip system by

$$\text{curl}\left(\mathbf{F_p}\right) = \sum_{i=1}^{n} \mathbf{\Lambda^i} \rho_{gnd}^i \tag{1}$$

129 where $\mathbf{\Lambda^i}$ is the second order tensor that holds the slip system geometry information (details in

130 Dunne et al. (2012)) and ρ_{GND}^i the GND density on slip system i.

131 The microstructure-sensitive stored energy density methodology presented by Wan et al.

132 (2014), argued that 5% of energy due to plastic deformation is stored as dislocation structures

133 and 95% is dissipated as heat. They derived the accumulated stored energy density G_{SE} at each

134 microstructural point as

$$G_{SE} = \int \frac{\zeta|\boldsymbol{\sigma}:d\boldsymbol{\varepsilon}^p|}{\sqrt{\rho_{SSD} + \sum_{i=1}^{n} \rho_{GND}^i}} \tag{7}$$

135 in which ζ represents the fraction of plastic energy stored locally, i.e. $\zeta = 0.05$. The stored

136 energy criterion has been extensively used to study crack nucleation and growth, and therefore

137 to predict the fatigue life of materials [Chen et al. (2018), Wilson et al. (2019)]. In the present

138 work, the accumulation of stored plastic energy in the material by the creation and evolution

139 of dislocation structures is argued to be a key factor for twin nucleation. In the context of

140 deformation twinning, the accumulation and dissociation of dislocations at the grain boundaries

141 lead to the formation of twin nuclei [Jeong et al. (2018)]. Hence local stored energy density

142 considered also by other authors [Capolungo and Beyerlein (2008), Cheng and Ghosh (2015),

143 Cheng and Ghosh (2017)] is investigated, but here the particular form of energy in eqn. (7) is

144 that stored by dislocation structure within an area determined by the dislocation density. The

145 underpinning dislocation mechanistic basis is described in Zheng et al. (2019) and it is noted

146 that the energy is stored predominantly by geometrically necessary dislocations.

147 **3. Results**

148 **3.1 Deformed microstructure and experimental twin variant identification**

149 Fig. 1(a) shows the microstructure before deformation with average grain size of 80 μm, where

150 the highlighted dashed square indicates the section of microstructure considered for CPFE

151 analysis and solid square indicates the region of interest (ROI) for HR-EBSD analysis. The

152 deformed microstructure in the ROI (Fig. 1(b)), along with the HCP unit cells to indicate the

153 grain orientations with respect to loading direction (TD), shows the presence of deformation

154 twins with low area fractions. The primary observation is that twinning is not activated in the

155 grain with most favourable crystallographic orientation for twinning (Grain P), but instead it is

156 active in surrounding grains with least favourable crystallographic orientations. These grains

157   are henceforth referred to as grains A, B, C and D as shown in Fig. 1(b). In order to investigate

158   twin nucleation, it is necessary to locate twin tips in these grains. Among grains A-D, the twin
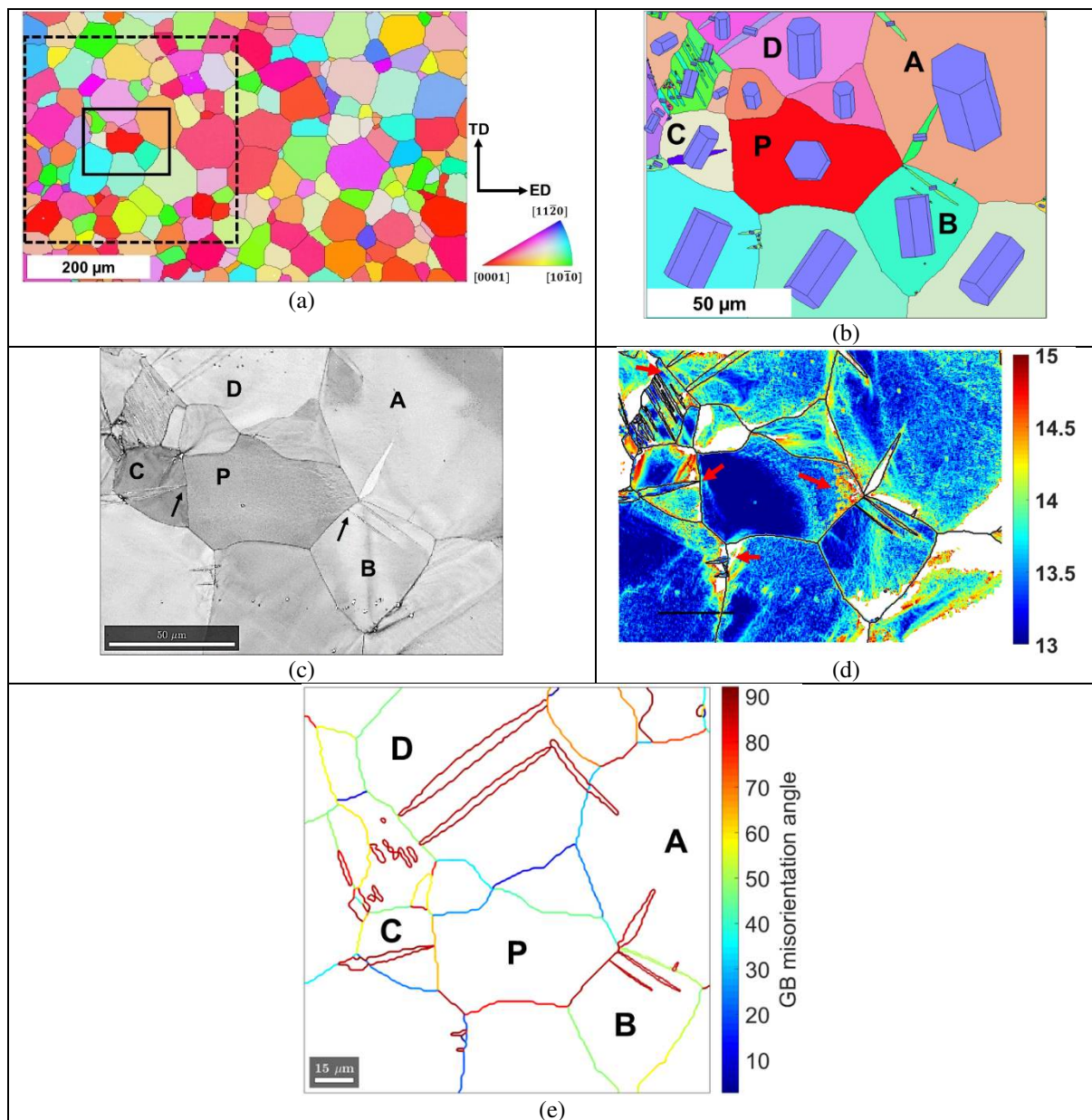

Figure 1: Uniaxial compression results showing (a) Undeformed microstructure, where the dashed square indicates the region of interest (ROI) for CPFE simulations and the solid line square indicates ROI for HR-EBSD analysis, (b) the ROI for HR-EBSD analysis after deformation with unit-cell orientations, (c) image quality map of the ROI and (d) GND density distribution in the ROI, where the red arrows show high GND density at twin tips (e) Grain boundaries (GB) of grains A-D and P showing misorientation angle

159

160   tips in grain C (right-hand tip) and B (left-hand tip) appear uncertain (see Fig. 1(b)). Therefore

161   the image quality map (Fig. 1(c)) of the EBSD data is investigated, which confirms that the

9

162

tips of these twins in grain C and B are indeed at the respective parent grain boundaries

(indicated using black arrows in Fig. 1(c)). Fig. 1(d) shows the distribution of GND density in

the microstructure shown in Fig. 1(b). The GND distribution is heterogeneous within the grains

and in particular at the vicinity of deformation twins, with high density at the twin tips

(indicated using red arrows) compared to their respective twin boundaries. Fig. 1(d) also shows

heterogenous distribution of GND density within the twin of grain C. It is shown in several

studies that nucleation of twins at the high angle grain boundaries is typically assisted by local

dislocations (slip-assisted), where the local high stress fluctuations drive twin nucleation and

variant selection [Beyerlein et al. (2010), Beyerlein et al. (2011), Khosravani et al. (2015)].

Fig. 1(e) shows the grain boundary misorientation angles in the region of interest comprising

grains A-D and P. One of the twins in grain A, which shares a boundary with grain D, appears

to have nucleated at the grain boundary with a misorientation angle of ~35°. This

misorientation angle and the presence of an adjoining twin in neighbouring grain D indicates

that these twins may have nucleated through twin-assisted-twinning, which is consistent with

independent studies [Khosravani et al. (2015)]. In contrast, the other twin in grain A that shares

the boundary with grain B and P, appears to have nucleated close to the triple junction. Twins

in grains B-D have nucleated at grain boundaries with higher misorientation angles (>40°),

indicating that these are slip-assisted nucleation events.

There are six variants of extension twins (variants of $\{10\bar{1}2\}\langle10\bar{1}1\rangle$) as shown in Table 1,

therefore the next step is the identification of variant type of the twins in grains A-D. There are

several methods to identify the twin variants such as by trace and orientation analysis [Jiang

et al. (2008), Pei et al. (2012)]. In the current study the method of orientations is employed,

where the crystallographic orientations of all six twin variants corresponding to parent grain

orientation are calculated using the procedure outlined in [Niewczas (2010)]. Then the

Table 1: Extension twin variant types

Variant type	Crystallography
1	$(10\bar{1}2)[\bar{1}011]$
2	$(01\bar{1}2)[0\bar{1}11]$
3	$(\bar{1}102)[1\bar{1}01]$
4	$(\bar{1}012)[10\bar{1}1]$
5	$(0\bar{1}12)[01\bar{1}1]$
6	$(1\bar{1}02)[\bar{1}101]$

187

188   experimentally measured twin orientations are compared with these theoretical ones to identify

189   the active variants in the microstructure. Fig. 2 shows the basal pole figures consisting of

190   numerical and experimental twin orientations corresponding to grains A-D. Following the

191   procedure briefed earlier, the active variants are identified as variant 1 in grains A, B and D,
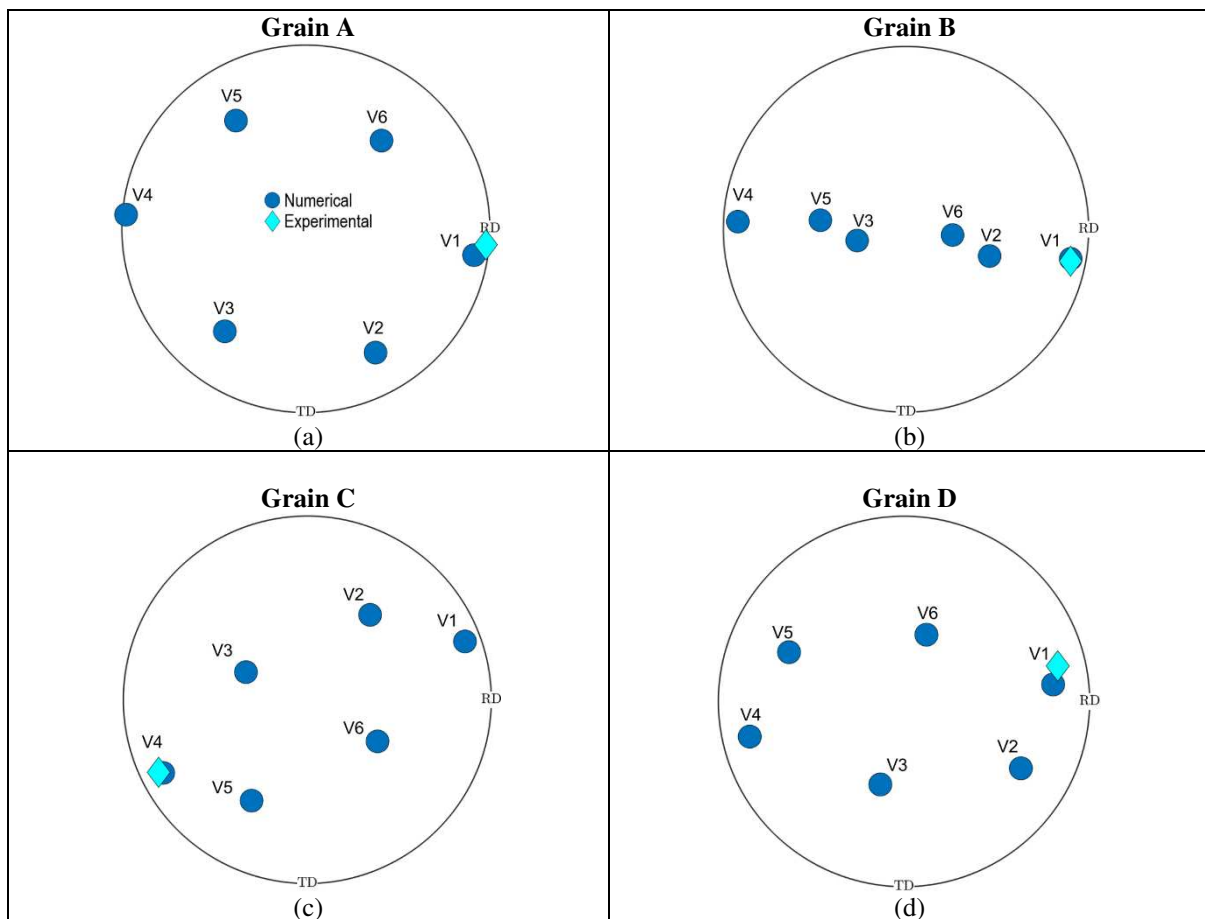

Figure 2: Discrete basal pole figures showing the numerical (blue dots) and experimental (diamonds) crystallographic orientations of twins in (a) Grain A, (b) Grain B, (c) Grain C and (d) Grain D. V# stands for variant (V) of type #.

192

193

while it is variant 4 in grain C. For the sake of completeness global Schmid factors, which rely on macroscopic loading direction, are also calculated to identify the type of twin variant active in the microstructure. Table 2 shows the Bunge Euler angles and global Schmid factors of all six variants of grains A-D, where the variants in bold are the active twin variants in the microstructure. From the table, except for grain C the global Schmid factors of active twin
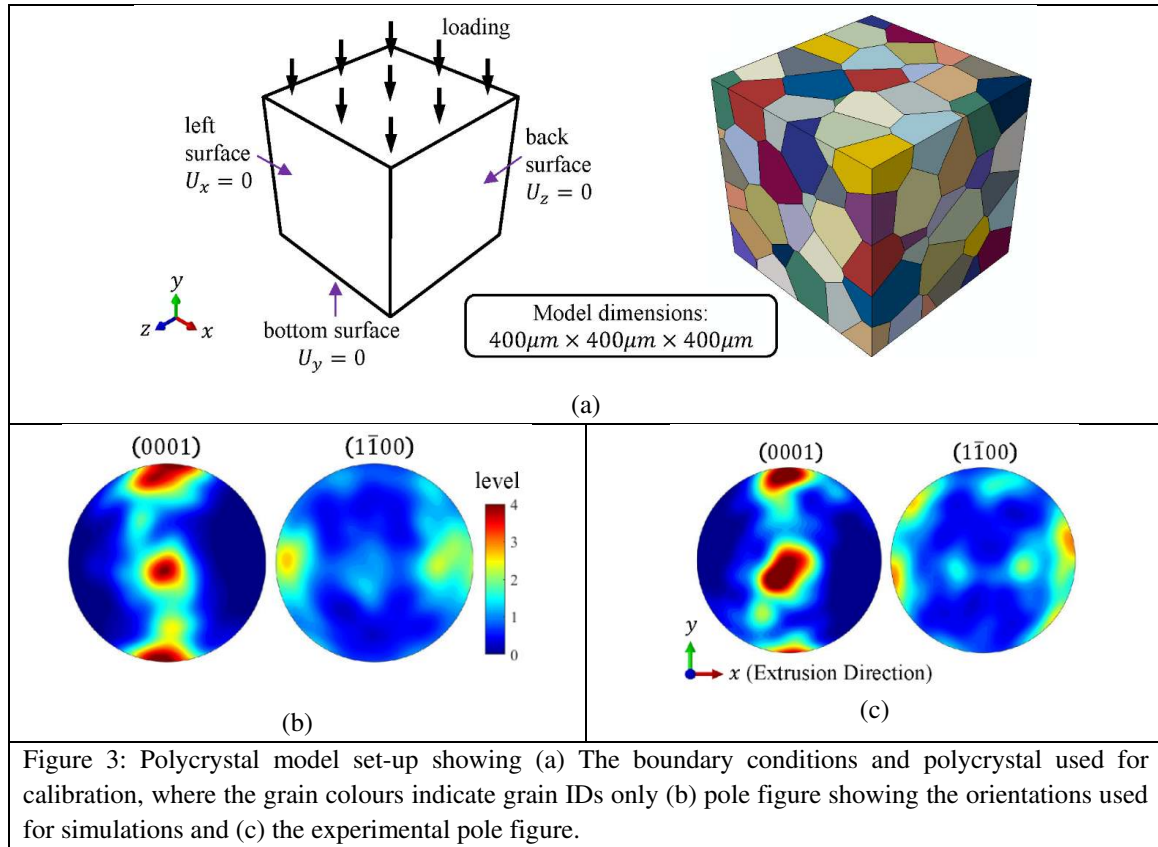
Table 2: Global Schmid factors of twins, where bold indicates active twin variants

Grain ID	Euler angles			Global Schmid factors					
				Variant 1	Variant 2	Variant 3	Variant 4	Variant 5	Variant 6
A	194	36	171	**-0.15**	0.16	0.07	-0.16	0.09	0.02
B	187	86	171	**-0.48**	-0.47	-0.49	-0.49	-0.49	-0.49
C	150	161	193	0.17	0.37	-0.01	**0.20**	0.41	0.00
D	183	56	158	**-0.34**	-0.25	-0.16	-0.32	-0.29	-0.22

variants are all negative. Deformation twinning is a 3D unidirectional defect as opposed to slip. This implies that the global Schmid factors of active twin variants should always be positive. Therefore, the global Schmid factors fail to explain the nucleation and selection of twin variants in grains A, B and D. In the case of grain C non-Schmid twin variant selection is followed, where the variant corresponding to the third rank is selected. The other alternative explanation for the nucleation of these twins is the activation by fluctuations of local (favourable) stress states, which is now explored further.

3.2 Model material property determination

In order to determine the slip rule (eq. 3) properties for subsequent modelling, a three-dimensional polycrystalline CPFE model comprising 125 grains as shown in Fig. 3(a) was used. The grain morphologies were generated using 3D Voronoi tessellation software VGRAIN [Zhang et al. (2011)] with the average grain size of 80µm to be representative of the experimental microstructure, which are then discretised using C3D20R finite elements. The

12

Figure 3: Polycrystal model set-up showing (a) The boundary conditions and polycrystal used for calibration, where the grain colours indicate grain IDs only (b) pole figure showing the orientations used for simulations and (c) the experimental pole figure.

213

214 crystal orientations were assigned from the EBSD map of the undeformed sample. The overall

215 texture represented in the model and recorded from the experiment are shown in Fig. 3(b) and

216 (c). Only 12 of the total 30 available slip systems $\{0001\} < 11\bar{2}0 >$, 3 prismatic slip systems

217 $\{10\bar{1}0\} < 11\bar{2}0 >$, 6 pyramidal slip systems $\{\bar{1}\bar{1}22\} < 11\bar{2}3 >$ - are considered in the current

218 study. The elastic stiffness tensor is defined as C_{11}=58.0, C_{12}=25.0, C_{13}=20.8, C_{33}=61.2,

219 C_{44}=16.6 (GPa) [Tromans (2011)]. The material properties following the calibration process

220 are listed in Table 3. The rate sensitivity parameters close to those experimentally measured by

221 Bhattacharyya et al. (2016) are used in this study, where the activation volume of basal and

222 prismatic slip is 100 b^3 and that of pyramidal slip is 6.25 b^3. The Debye frequency of Mg is

223 calculated to be ~1.2×10^{13} s^{-1} [Kwak et al. (2016)].

224

225

Table 3: Single crystal parameters for WE43 at room temperature

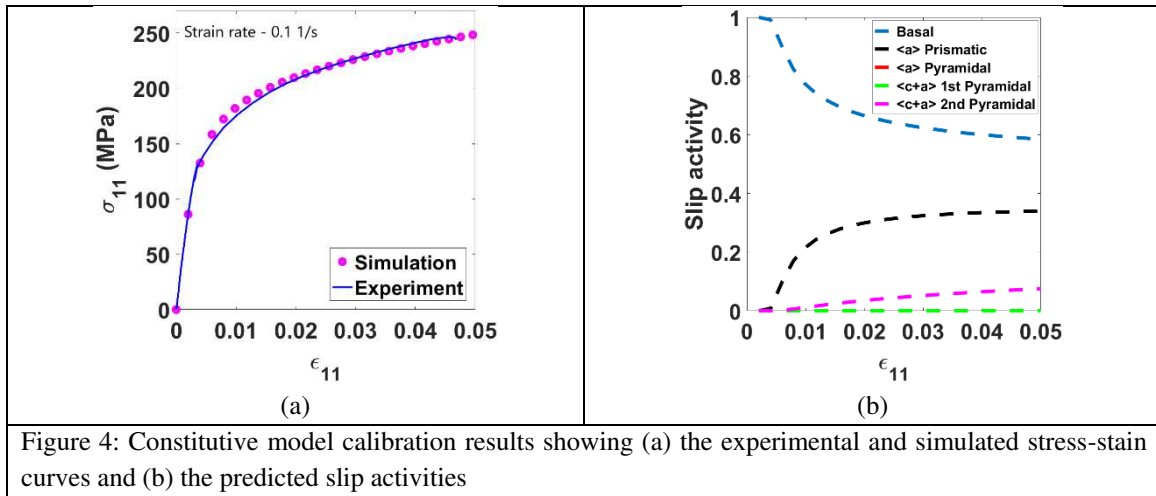| Mode	τ_{c0} (MPa)	ΔV (b^3)	ΔF (J)	ρ_m (μm^{-2})	V_D (s^{-1})	γ' (μm^{-2})	α
Basal	14	100					
Prismatic	72.8	100	7.4×10^{-20}	1	1.2×10^{13}	1000	0.75
Pyramidal II order	126	6.25					

226

Figure 4: Constitutive model calibration results showing (a) the experimental and simulated stress-stain curves and (b) the predicted slip activities
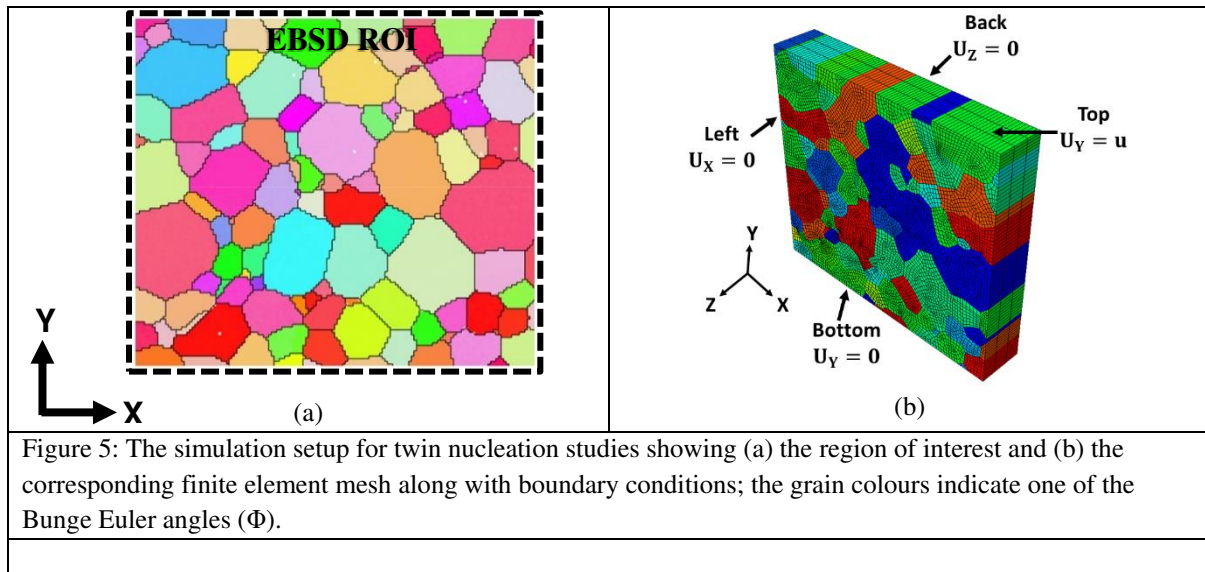
227

Fig. 4(a) shows the experimentally measured macroscopic true stress-strain response and the corresponding CPFE calculated response that shows good agreement with experiments. The slip activities during deformation are shown in Fig. 4(b). During compression, the basal slip system is activated first and is dominant at the onset of plastic deformation. Its activity decreases gradually with an increase in the contribution of other slip systems. Similar trends have been reported in independent studies (e.g. Bhattacharyya et al. (2016)).

3.3 Crystal plasticity analysis of twin nucleation

As discussed in section 3.1, global Schmid factors fail to explain the observed activation of twins. Therefore, the section of microstructure (Fig. 1(a)) including the grains of interest is explicitly replicated in the CPFE geometric model to study the local stress fields that may have
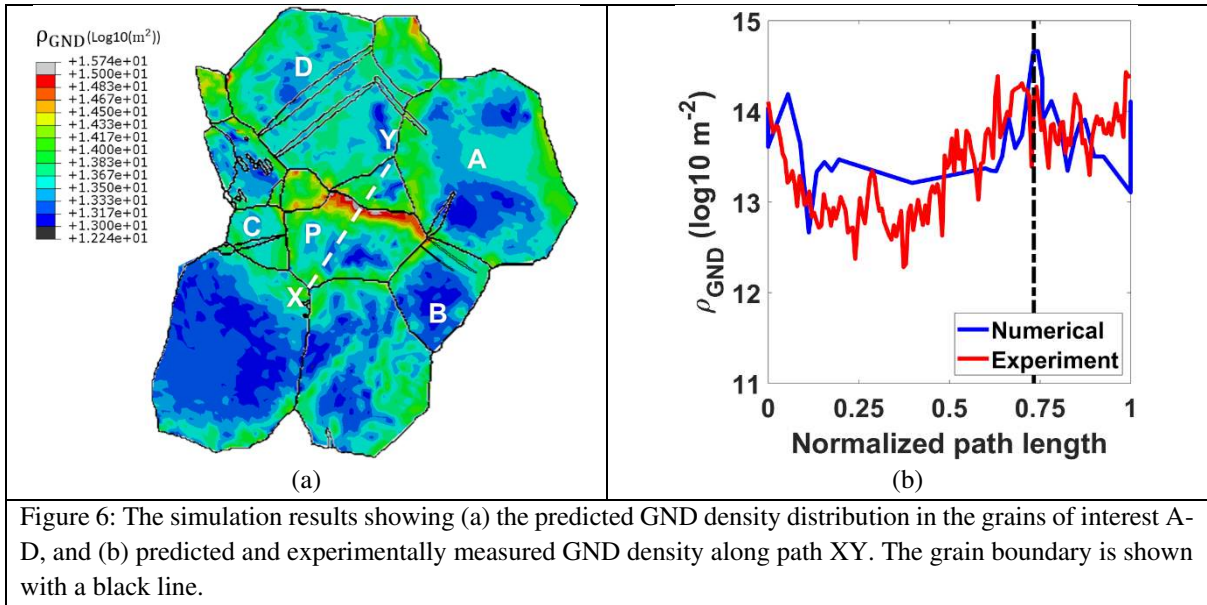
238 facilitated twin nucleation (prior to their incipient formation). Fig. 5(a) shows the

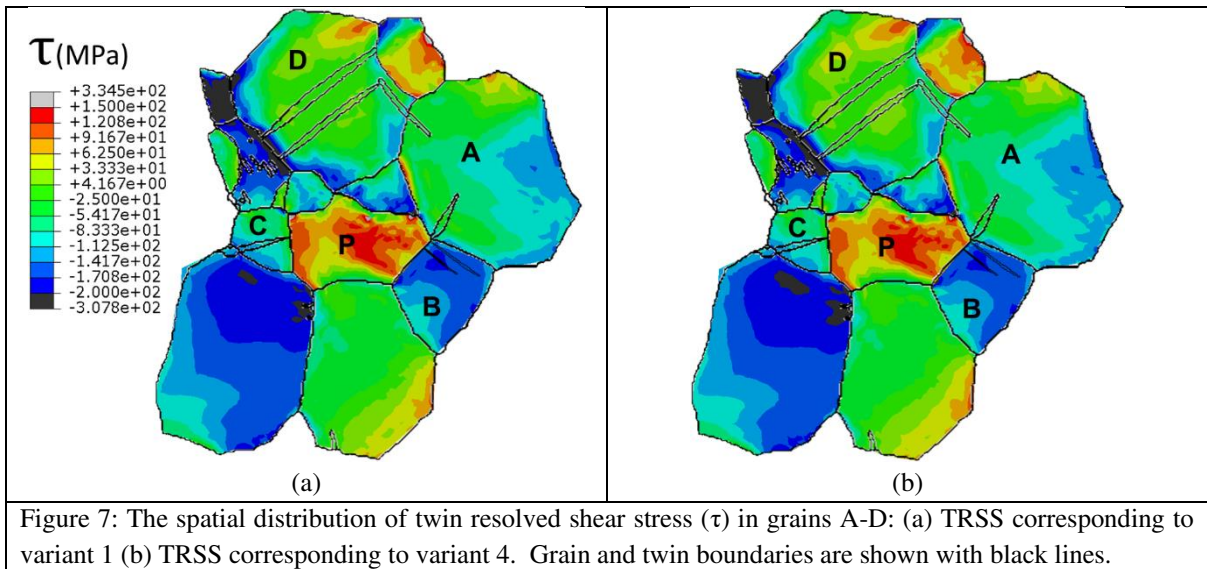239 microstructure and Fig. 5(b) the corresponding finite element mesh, which has an area of

Figure 5: The simulation setup for twin nucleation studies showing (a) the region of interest and (b) the corresponding finite element mesh along with boundary conditions; the grain colours indicate one of the Bunge Euler angles (Φ).

240

241 446×397 μm^2 and thickness 80 μm. Note that we proactively replicate the experimental

242 microstructure prior to the nucleation of twins, which are not, therefore, explicitly represented

243 in the geometric model, since this establishes the stress states leading to twin nucleation. A

244 limitation of the current approach is that the 2-D microstructure is extruded in the Z-direction

245 to obtain a pseudo 3-D model, which does not contain sub-structure information. Many studies

246 have shown that the sub-surface microstructure influences the spatial distribution of

247 deformation fields [Zeghadi et al. (2007), Zhang et al. (2018)]. However, Zhang et al. (2018)

248 have also shown that the presence of the sub-surface mostly only influences the magnitudes of

249 GND density, relative lattice rotations and strain fields but does not alter the observed trends

250 on the free surface. The model is loaded along direction Y (corresponding to TD) until 5%

251 strain at the strain rate of 0.1 s^{-1}. Once this strain is reached, the model is unloaded.

252 Fig. 6(a) shows the calculated GND distribution within the grains of interest, where the CPFE

253 geometric model is superimposed with the experimental grain boundaries to indicate twins and

254 path XY indicates that along which GND density is measured. The distribution of GND density

Figure 6: The simulation results showing (a) the predicted GND density distribution in the grains of interest A-D, and (b) predicted and experimentally measured GND density along path XY. The grain boundary is shown with a black line.

255

256 along the path XY is shown in Fig. 6(b), in which the CPFE satisfactorily captures the

257 experimental trends. Twin nucleation has in the literature been attributed to local stress states,

258 where a twin nucleates when the (positive) RSS driven by local stress states reaches the CRSS

259 of the particular twin type. Therefore, RSS is calculated here at the peak applied strain and

260 examined for the active twin variants in grains A-D; that is, variants 1 and 4. Fig. 7(a) shows

261 the spatial distribution of TRSS for variant 1, while Fig. 7(b) shows that for variant 4. The

Figure 7: The spatial distribution of twin resolved shear stress (τ) in grains A-D: (a) TRSS corresponding to variant 1 (b) TRSS corresponding to variant 4. Grain and twin boundaries are shown with black lines.

262

16

263   RSS in grain P is predominantly positive as expected considering the favourable

264   crystallographic orientation, but this grain does not nucleate any twins. Another observation is

265   that the RSSs corresponding to variant 1 (Fig. 7(a)) and variant 4 (Fig. 7(b)) are largely negative

266   within grains A-D. This is also expected as the grain orientations (Table 2 and Fig. 1(b)) are

267   least favourable. However, these are the grains within which twins are observed to nucleate,

268   contrary to convention based on resolved shear stress for extension twins. This implies that the

269   nucleation of these twins is not driven by local stresses that lead to high resolved shear stresses.

270   Therefore, the concept of twin nucleation based on CRSS (stress driven) does not explain the

271   activation of these twins in the microstructure. Nor does it explain the absence of twin

272   formation in grain P.

273   Fig. 8 shows the spatial distribution of effective plastic strain and basal, prism and pyramidal

274   slip respectively developed in grains A-D. The plastic strain and corresponding slip fields are

275   heterogeneous with some relationship to the twin nucleation sites within the grains A, B and

276   D. In particular, for grain A, one of the twins appears to nucleate from a location of high basal

277   slip. For grain B, a high localised pyramidal slip and local basal slip is potentially related to

278   twin nucleation, where the former is seen to make a considerable contribution to the effective

279   plastic strain compared to other slip systems. Grain C shows a localised region of high basal

280   slip on the right-hand boundary region close to where the narrow twin section is observed

281   (suggesting nucleation end). For grain D, it's again basal slip which seems potentially to be

282   related to both twins nucleating within this grain.

283   In summary, therefore, the hotspots in slip/plasticity are observed to have some relationship

284   to observed twin nucleation occurrences in this microstructure, but it by no means precisely

285   and unambiguously locates the twin nucleation sites in all cases. The study of local quantities

286   within the microstructure from the CPFE compared with experimental observations therefore

287   seem to suggest that while local GND density, resolved shear stress and accumulated slip are
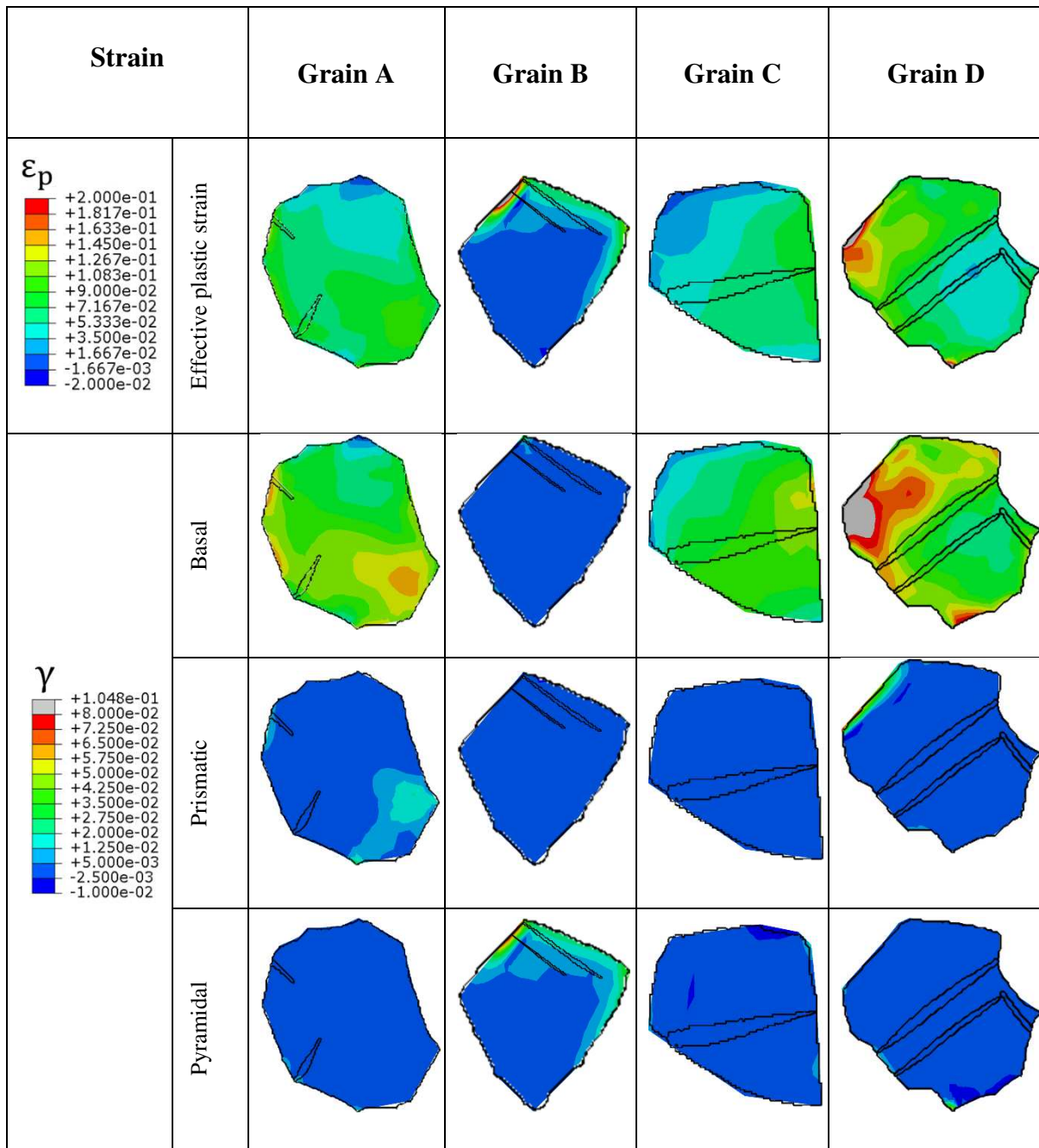
Figure 8: The spatial distribution of predicted effective plastic strain and the basal, prism and pyramidal slip fields in grains A-D as shown. Grain and twin boundaries are shown with black lines.

288

relevant and locally important to nucleating twins, they are not in their own right deterministic predictors of nucleation. We therefore turn to the energy approaches discussed in the introduction and in particular consider the dislocation-moderated stored energy density given in eqn. (7).

293   Fig. 9 (a)-(d) (i) shows the spatial distribution of stored energy density within grains A-D.

294   Dashed lines indicate paths along which stored energy density is extracted for line-graph plots

295   in (ii). Qualitatively, the stored energy density is observed to be consistently high within parent

296   grains at the twin nucleation sites. For instance, observe the high stored energies within grains

297   B and D in Fig. 9(b)(i) and Fig. 9(d)(i) at the vicinity of the twin nucleation sites.

298   Fig. 9 (a)-(d) (ii) shows the extracted stored energy densities measured along the paths shown

299   (Fig. 9(i)) in grains A-D respectively, in which the black vertical lines indicate the

300   experimentally observed twin nucleation sites. In grain A two twins are identified as AT1 and

301   AT2, where the nucleation of AT1 appears to be slip assisted while AT2 (dashed line in Fig. 9

302   (a)(ii)) seems to be related to the secondary twin in grain D (see Fig. 7)). The focus, therefore,

303   is on nucleation of AT1 but for the sake of completeness AT2 is also shown. From Fig. 9(a)(ii),

304   the experimental nucleation site of AT1 corresponds to the highest stored energy along path

305   P1-P2. Similarly for grain B in Fig. 9(b)(ii), the distinct peak in the stored energy corresponds

306   to twin nucleation site BT2 in Fig. 9(b)(i) and twin BT1 nucleates close-by at a location also

307   with high stored energy. While the latter is apparently not the highest energy density, the

308   nucleation of BT2 is likely to perturb the distribution of energy density, and were the spatially

309   resolved twin formation to be explicitly incorporated in the modelling, it is perfectly feasible

310   that the subsequent highest energy location would shift (from BT2) to BT1. This phenomenon

311   (redistribution of energy density) has been explicitly demonstrated in the context of secondary

312   crack nucleation in other studies [Chen et al. (2017)]. In the case of grain C, the location of

313   peak energy density corresponds exactly to the twin nucleation site. The stored energy,

314   however, appears quite uniform along this particular grain boundary R1-R2 but again, once

315   twin CT1 has been nucleated, the distribution of energy density and its magnitude is likely to

316   be very different, and sufficiently dissipated to reduce the energy driver for additional twin

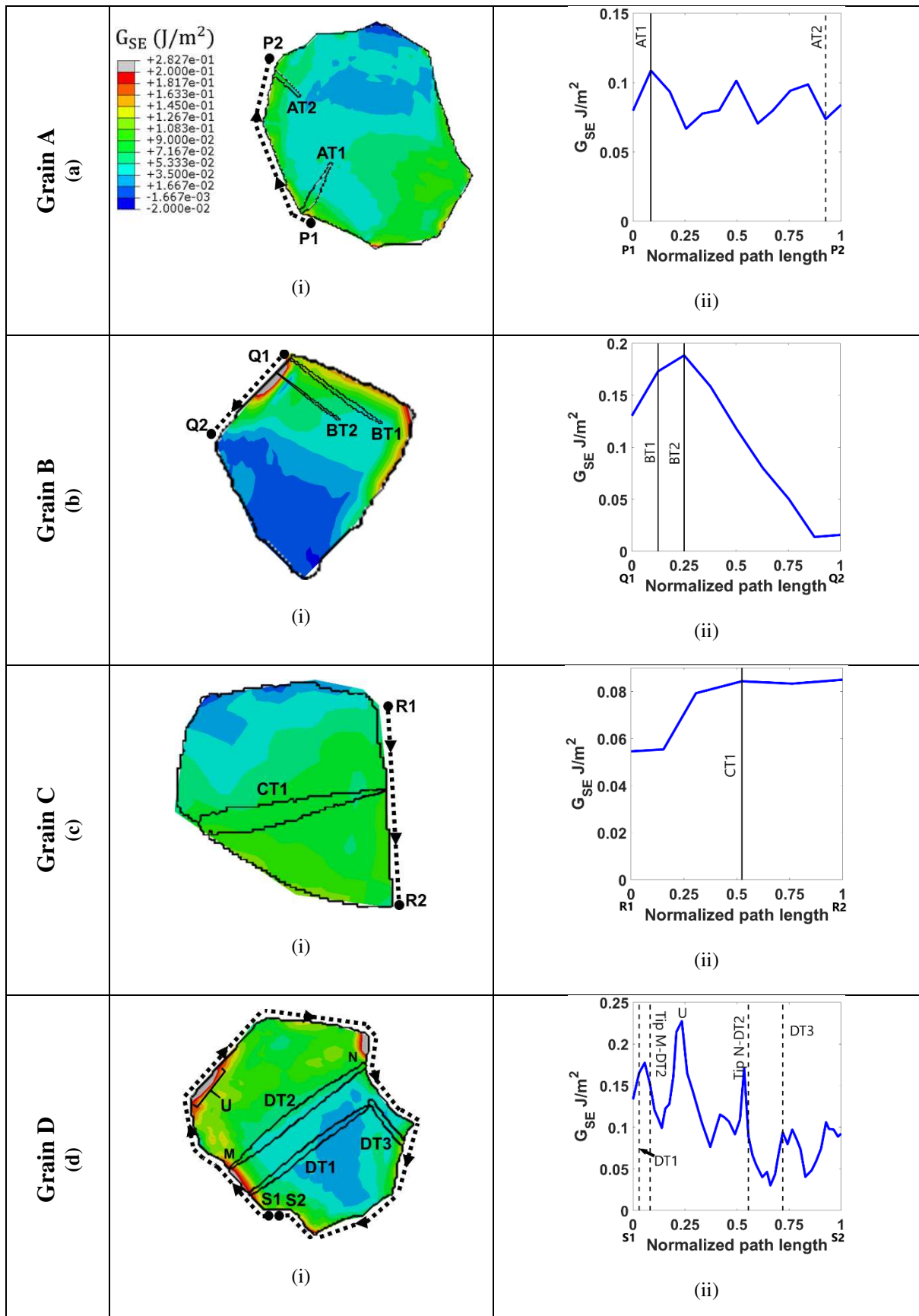317   nucleation anywhere else along this boundary.

Figure 9: The calculated stored energy density (i) spatial distribution and (ii) along the paths (dashed lines) indicated in (i) for grains (a) A, (b) B, (c) C and (d) D. The solid black lines indicate the slip-assisted twin nucleation sites along respective paths.

318   Grain D nucleates three twins identified as DT1, DT2 and DT3. Twins DT1 and DT2 appear

319   to have nucleated at the grain boundary by slip assisted nucleation, while DT3 seems to be

320   secondary twin-assisted nucleation. The analysis in Fig. 9(d)(i) of the energy density at the left-

321   most tip of DT1 shows high stored energy compared to the right-hand tip. Therefore, DT1

322   seems to have nucleated at the grain boundary. Twin DT2 also seems to originate from the high

323   stored energy density location (M) common with DT1, but it is the case that a further region of

324   high energy density is observed close to, but not at, the right-hand tip of twin DT2 (N). Fig.

325   9(d)(ii) shows the distribution of stored energy density measured along the path S1-S2 (Fig.

326   9(d)(i)). The energy density at the vicinity of location U (Fig. 9(d)(i)) is noted to be the highest

327   along path S1-S2 and yet no twin is observed to nucleate at this location. In all the cases of

328   slip-driven twin nucleation observed and analysed in this study, location U in grain D is the

329   only example of a higher stored energy density being calculated in the absence of the

330   observation of a twin nucleation. This observation, and the nucleation of twins DT1 and DT2

331   at energy densities lower than that in region U, is explicitly investigated later in section 3.4.

332   All the results in Fig. 9 are shown for the peak applied strain (5%) such that any one value of

333   peak stored energy density should not be inferred as a *critical* value to drive twin nucleation.

334   Indeed, experimental observation suggests that in the alloy considered, twin nucleation initiates

335   early in the loading history at about 100 MPa [Guan et al. (2019)], corresponding to an applied

336   strain of about 0.002 (Fig. 4(a)). Hence, in order to extract out a definitive critical stored energy

337   density required to cause twin nucleation, it is necessary to have knowledge of the calculated

338   energy density at the point in the loading history when twin nucleation at a specific location is

339   observed.

340   The peak energy densities extracted for grains A to D at applied peak strain of 5% (from Fig.

341   9 (ii)) are of order 0.11, 0.2, 0.08, and 0.175 Jm^{-2} respectively, such that a critical value must

342   therefore be 0.08 Jm^{-2} (corresponding to grain C) or less. The full histories of the energy

densities at each of the key locations of twin nucleation can be extracted from the crystal plasticity analysis. On the basis that first twin nucleation was observed by Guan et al. (2019) at an applied stress of 100 MPa (corresponding to an applied strain of ~0.2%), it becomes possible to estimate the *critical* value of stored energy for twin nucleation using the model results for grain C, and the critical stored energy is estimated to be 0.015 Jm^{-2}. The absence of twins in grain P is notable, since this grain is apparently well-orientated and anticipated to nucleate twins. However, the accumulation of grain-averaged stored energy density with applied strain in grains A-D and P is shown in Fig. 10. From this figure, the accumulation is the least in grain P compared to grains A-D. Hence while twin nucleation criteria based on global Schmid factor and resolved shear stress would indicate grain P should twin, the stored energy density does not, in agreement with experimental observations. In addition, it is noted that grains A-C are immediate neighbours of grain P (Fig. 1(b)), wherein grains A and C nucleate twins much earlier in the deformation history. Hence it is argued that the nucleation of twins in grains A-D, as a consequence of higher accumulation of stored energy, relaxes and redistributes the energy such that grain P never attains the *critical* energy density.
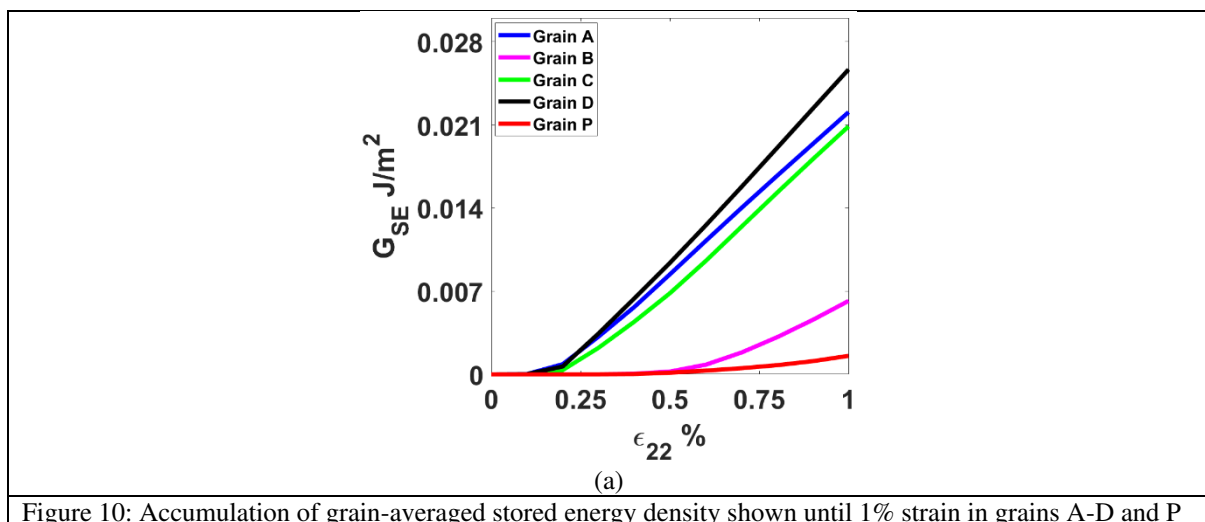

(a)

Figure 10: Accumulation of grain-averaged stored energy density shown until 1% strain in grains A-D and P

3.4 Twin variant selection analysis

The experimental observations in the current study indicate that neither the global Schmid factor nor the twin RSS analyses explain the twin nucleation and variant selection (Table 2 and Fig. 7) observations. Hence the geometric compatibility factor and shear strain accommodations are firstly explored to study the twin variant selection observations in grains A and B.

3.4.1 Geometric compatibility factor and shear strain accommodation analysis

Similar to slip transfer through interfaces, the geometric compatibility (m') between twin and slip can be defined as [Luster and Morris (1995)]

$$m' = \cos\varphi \times \cos\omega \tag{8}$$

where φ and ω are the angles between plane normal and shear direction of slip system in the neighbouring grain and twin systems in parent grain respectively. High m' means the slip system is well aligned with the twin variant and vice versa. The likelihood of strain transfer across the grain boundary by the nucleation of a twin in the parent grain increases as the value of m' approaches unity, while a low value (~0) of m' implies that the grain boundary is impenetrable. However, in the present experimental study the parent grain crystallographic orientations (A-D) are less favourable for twinning. Therefore, the value of m' is expected to be low compared to other independent studies.

The selection of non-Schmid twin variants by the parent grain has also been explained in the independent literature (e.g. [Jonas et al. (2011)]) on the basis of shear strain accommodation. In that work, the twin variant selected within the parent grain is expected to be that which requires least strain accommodation by prismatic slip and the highest by basal slip in the neighbouring grain. However, these studies were performed with grains that are favourably

23

384   oriented for twinning, which generate twins at lower strains and largely activate basal slip. In

385   the current study both the prismatic and basal slip collectively accommodate strain post-yield

386   (Fig. 4(b)). Therefore, the total ⟨a⟩ type shear is considered containing contributions from both

387   basal and prismatic slip. Thus, in this study, we firstly assess the criterion for variant selection

388   within the parent grain which is based on maximum ⟨a⟩ type shear accommodation in the

389   neighbouring grain in order to put the current work in the context of that in the open literature.

390   In addition, it transpires that the shear accommodation hypothesis and m′ do not work. Hence

391   this is followed by the introduction of a new shear energy density criterion.

392   Following the procedure outlined in Jonas et al. (2011), the determination of accommodation

393   strains involve defining a displacement gradient tensor $\mathbf{S}$ in the twin reference frame, where

394   the X, Y and Z directions correspond to the shear direction, the shear plane normal, and the

395   cross product of X and Y directions respectively. All the components of $\mathbf{S}$ except the $\partial u / \partial z =$

396   s are zero, where s is the characteristic shear associated with a twin system (0.129 for extension

397   twins). The tensor $\mathbf{S}$ is given as

398
$$\mathbf{S} = \begin{pmatrix} 0 & 0 & s \\ 0 & 0 & 0 \\ 0 & 0 & 0 \end{pmatrix} \tag{9}$$

399   This displacement gradient tensor is then rotated onto the crystallographic reference frame of

400   the neighbouring grain to result in a new displacement gradient tensor e_{ij}, which contains all

401   nine non-zero components. The non-zero shear components are given a physical interpretation

402   in terms of the amount of shear strain required on a deformation mode in the neighbouring

403   grain to accommodate the formation of a twin variant in the parent grain [Jonas et al. (2011)].

404   Therefore, the main focus is on the shear components that correspond to shear on basal and

405   prismatic slip systems. In particular the shear on the basal slip is determined as $\left(|e_{xz}| + |e_{yz}| \right)$,

406   on prismatic slip is $\left(|e_{xy}| + |e_{yx}| \right)$ and finally the summation from shear on basal and prismatic

407   is the total ⟨a⟩ type shear.

408 Table 4 and 5 show the shear strains accommodation and m′ for all six possible twin variants

409 for grains A and B respectively. The experimental results show that the twin variant 1 is

410 selected by grain A (Fig. 2(a)). From Table 4, variants 1 and 6 have the maximum shear

411

Table 4. Shear accommodation and m′ analysis of Grain A (bold indicates the observed active variant)

Twin variants	Shear accommodation			m′	
	Basal	Prismatic	⟨a⟩ type	Basal	Prismatic
1	**0.14**	**0.07**	**0.21**	**0.41**	**0.28**
2	0.04	0.09	0.13	0.64	0.09
3	0.00	0.02	0.02	0.52	0.22
4	0.02	0.07	0.09	0.23	0.26
5	0.11	0.06	0.17	0.04	0.07
6	0.16	0.05	0.21	0.11	0.20

416 accommodation but among these two variants, the geometric compatibility factors for both

417 basal and prismatic slip systems of variant 1 are greater than that of variant 6. Therefore, the

418 preferred variant for grain A based on the two criteria is variant 1.

419 In grain B, the experimental active variant is also variant 1 (Fig. 2(b)). Among all the available

420 six variants (Table 5), the 1st, 4th and 5th variants possess the same shear strain

421 accommodation from the neighbouring grain, which means that these variants are equally

422 probable.

Table 5. Shear accommodation and m′ analysis of Grain B (bold indicates the observed active variant)

Twin variants	Shear accommodation			m′	
	Basal	Prismatic	⟨a⟩ type	Basal	Prismatic
1	**0.08**	**0.11**	**0.19**	**0.21**	**0.49**
2	0.07	0.11	0.18	0.39	0.30
3	0.07	0.06	0.13	0.30	0.25
4	0.08	0.11	0.19	0.11	0.49
5	0.08	0.11	0.19	0.22	0.32
6	0.09	0.04	0.13	0.16	0.21

427

428 From the corresponding m′ values, among variants 2, 4 and 5, variant 2 and 4 have the higher

429 compatibility offered by prismatic slip, while variant 5 has the highest for basal slip and the

430 least for prismatic slip. Therefore these two techniques lead to uncertainty in predicting the

431 active variant in grain B.

432 In summary, the shear strain accommodation and m′ factors have been considered to

433 investigate the variant selection in parent grains A and B but transpiring only to be partially

434 correct. The values of m′ depend on the 'alignment' of slip systems in the neighbouring grains

435 with the twin variant in the parent grain. The low values of m′, as reported in the current

436 investigation, have also been reported in independent studies [Wang et al. (2014), Liu et al.

437 (2016), Zhou et al. (2020)], which emphasize the importance of investigating the effect of local

438 deformation fields (stress, dislocation density etc.,) in twin variant selection. Zhou et al. (2020)

439 have shown that, in slip assisted twinning, it is necessary to consider the local slip activity

440 while predicting the twin variant selection using m′. Further, Wang et al. (2014) speculated

441 that the nucleation of twins (in one of their grains of interest) within the grains with negative

442 Schmid factor and low m′ may occur due to high local stresses at the grain boundaries. Thus,

443 we return to local stored energy density considerations to explain the experimental observations

444 that may correctly identify the variant selection in all the cases.

445 **3.4.2 Energy based investigation of variant selection**

446 In an earlier section, stored energy density was shown to identify correctly the locations of

447 experimentally observed twin nucleation sites, albeit with one location (region U) showing

448 high energies in the absence of observed twins. Fig. 11(a) shows a schematic representation of

449 one such location of high stored energy density (G_{SE}^{max}) in the parent grain along the grain

450 boundary that serves as a high energy and defect source for a twin embryo formation. In order

451 to assess variant selection, an appropriate energy density is also developed to account for the

452 energy stored in the parent grain due to formation of a given twin variant. Experimental data
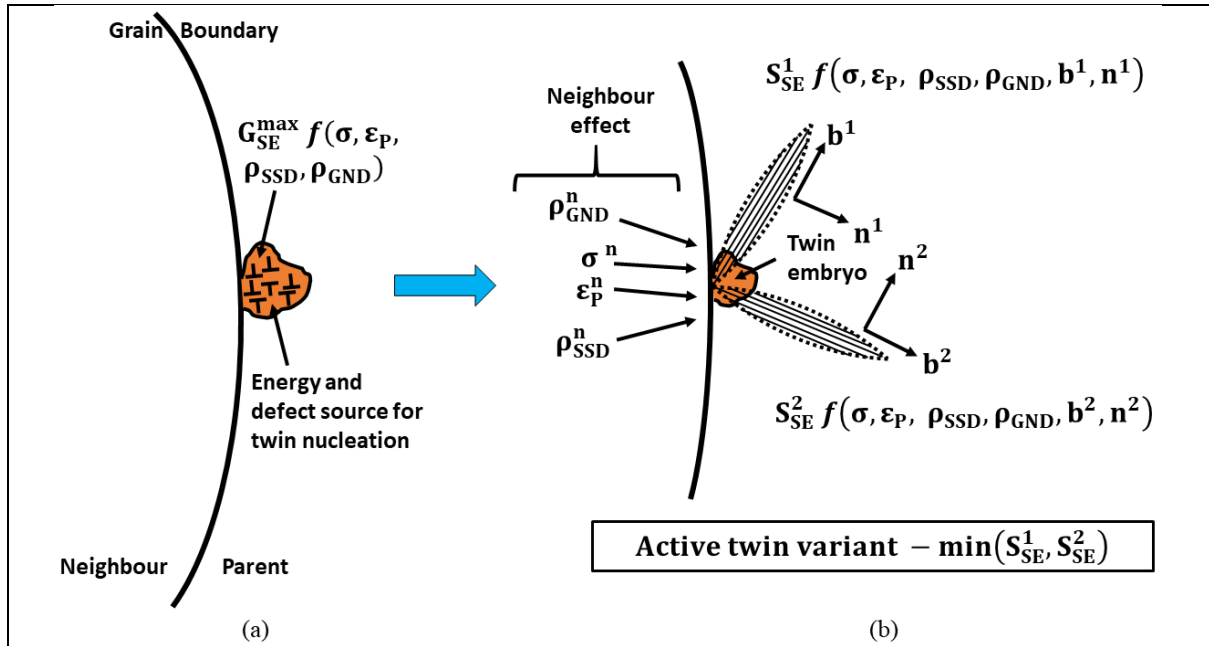
Figure 11: Schematic representation of twin nucleation and variant selection energy based criteria (a) location of high stored energy density (G_{SE}^{max}) along the grain boundary (b) twin variant selection criterion, operating at the location of G_{SE}^{max}, show only for 2 of 6 possible twin variants for the sake of clarity. S_{SE}^1 and S_{SE}^2 are the shear stored energy density of variants 1 and 2, and **b** and **n** are the twin shear direction and plane normal respectively.

reported in the literature show that the dislocation pile-up at the parent grain boundaries dissociate to form a twin nucleus, which further propagates and grows to form a twin. Therefore, the type of twin variant selected in the parent grain is decided at the incipient stage of nucleation at the parent grain boundaries. Beyerlein et al. (2011) have also observed a weak relationship between grain orientation and twin variant selection, and showed that the nucleation and variant selection are influenced strongly by the local high stress fluctuations at the grain boundaries. Hence an energy density term is established that is measured for all six twin variants at the parent grain boundaries to identify the twin variant.

It is shown in independent studies that a twin embryo forms by the dissociation of dislocations in the parent grain leading to formation of partials and twinning dislocations that shear the parent grain [Wang et al. (2009b)]. If φ^β is the total energy associated with the formation of an embryo of a twin variant β after the dissociation event, then this energy comprises that associated with the twin embryo (E_F^β) and work done (W_{ex}^β) by twinning dislocations

467 [Capolungo and Beyerlein (2008)]. This implies that the energy of the twin embryo (E_F^β) is

468 stored in the material, while the work done is dissipated (lost). Therefore the total energy is

469 given as [Nabarro (1952)]:

470 $$\varphi^\beta = E_F^\beta + W_{ex}^\beta \tag{10}$$

471 On a continuum scale, for a given stress state ($\boldsymbol{\sigma}$) and plastic strain state ($\boldsymbol{\varepsilon_P}$) at a given

472 microstructural location in the parent grain, the total energy associated with formation of a

473 given twin variant post dislocation dissociation event can be estimated as:

474 $$\varphi^\beta = (\boldsymbol{\sigma} : \mathbf{m^\beta})\,(\boldsymbol{\varepsilon_P} : \mathbf{m^\beta}) = \tau^\beta\,\gamma_P^\beta \tag{11}$$

475 where the plastic strain ($\boldsymbol{\varepsilon_P}$) is given as

476 $$\boldsymbol{\varepsilon_P} = \int_0^t \mathbf{\dot{d}\varepsilon_P}\,dt \tag{12}$$

477 and $\mathbf{m^\beta}$ is the symmetric part of the Schmid tensor defined as $\mathbf{m^\beta} = \frac{1}{2}\big((\mathbf{b^\beta} \otimes \mathbf{n^\beta}) +$

478 $(\mathbf{n^\beta} \otimes \mathbf{b^\beta})\big)$, where $\mathbf{n^\beta}$ and $\mathbf{b^\beta}$ are twinning plane normal and direction respectively, τ^β the

479 resolved shear stress and γ_P^β the resolved accumulated shear strain of twin variant β. When

480 dislocation pile up in a parent grain dissociates to form multiple twinning dislocations, they

481 tend to form several variants of the same twin type [Mendelson (1969)]. Therefore it is

482 necessary to determine the energies associated with all six twin variants to understand the

483 variant selection.

484 It is shown in molecular dynamics studies that a stable twin embryo consists of either twinning

485 dislocations only or twinning and partial dislocations [Wang et al. (2009a)] that extend to a

486 thickness of several crystallographic planes [Wang et al. (2009b)]. Therefore in the present

487 formulation, a 3D representation of twin embryo is assumed that has a volume of ΔV_T, with an

488   area of A_T and length L_T, where the length L_T is taken to be the local dislocation mean free

489   distance λ. Thus the volume is given as

490    $$\Delta V_T = A_T L_T \; = \; \frac{A_T}{\sqrt{\rho_{SSD} + \sum_{i=1}^{n} \rho_{GND}^i}}$$

491   (13)

492   Then the shear energy density associated with the twin embryo that is stored in the system is

493   given as

494    $$S_{SE} = \frac{E_F^\beta}{A_T} \; = \; \frac{\varphi^\beta \Delta V_T}{A_T} \; = \; \frac{\tau^\beta \, \gamma_P^\beta}{\sqrt{\rho_{SSD} + \sum_{i=1}^{n} \rho_{GND}^i}}$$

495   (14) where the energy density associated with the twin embryo is called the shear stored energy,

496   S_{SE} and equates to the stored twin embryo energy E_F^β. Further, for the formation of a stable twin

497   embryo with an optimum distance between the twinning dislocations, the total energy

498   associated with the formation of a twin variant (φ^β) should always be a minimum [Capolungo

499   and Beyerlein (2008)], which implies that the energy of the twin embryo (E_F^β) should also be

500   minimised for the chosen variant. Therefore in the current study, this energy S_{SE} ($= E_F^\beta/A_T$)

501   is determined for all six twin variants at the parent grain boundaries where the total stored

502   energy density is maximum in order to identify that twin variant which has minimum energy

503   associated with its embryo formation. The schematic representation of one such twin embryo

504   formation event is shown in Fig. 11(b), where for the sake of clarity only two of six twin

505   variants are shown. At the location of peak G_{SE}^{max} location, it remains possible for any of the

506   possible six twin variants to form. The particular twin variant selected is argued to be that

507   which minimises the shear stored energy density (S_{SE}) for its formation compared with any

508   other variant.

509   Fig. 12 shows the shear stored energy density calculated for all the twin variants in grains A-

510   D, where this energy is measured along the same paths as the stored energy (Fig. 9(i)). For

511   grain B, the shear strain accommodation and m' compatibility analysis was shown not to result

512   in the correct observed variant selection, and that in fact twin variant 1 developed in this grain.

513   Examining grain B first, therefore, Fig. 12(b) shows that at the twin nucleation sites BT1 and

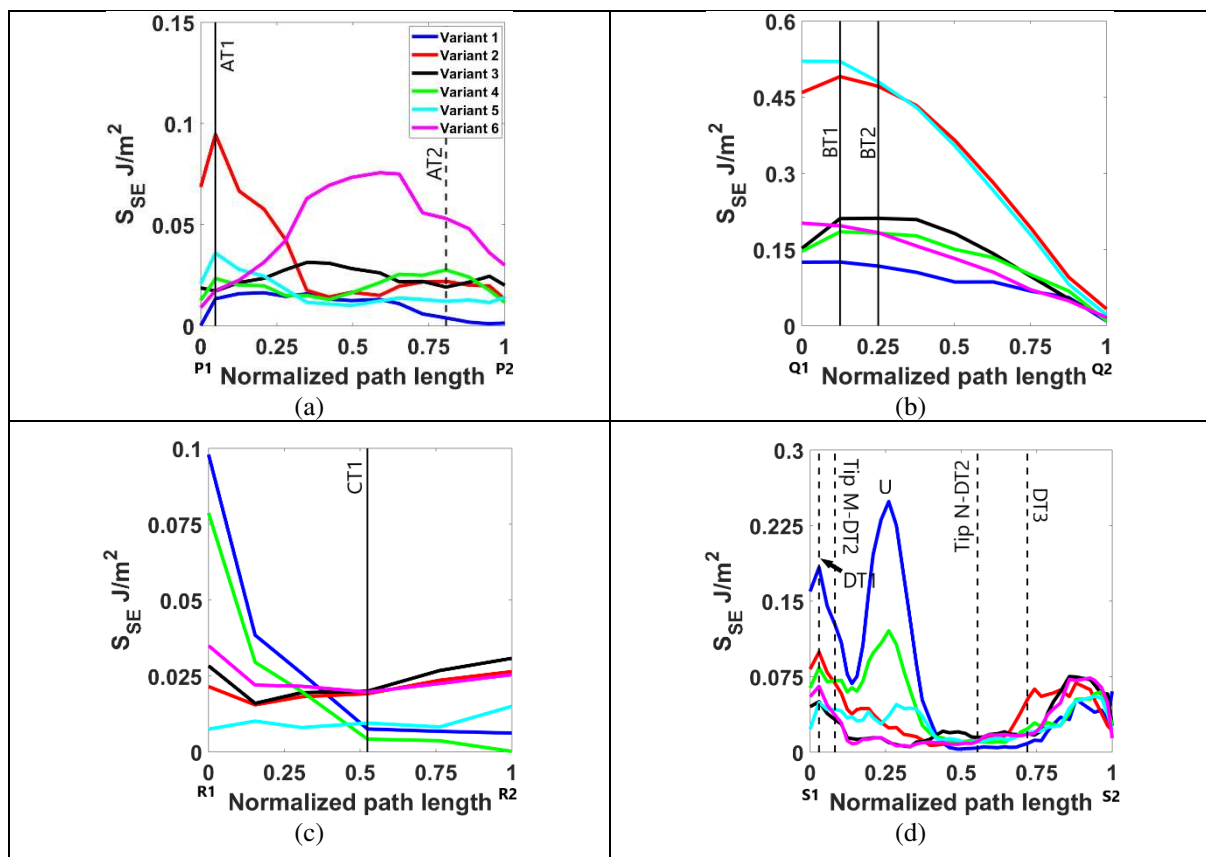514   BT2 (black lines) where the stored energy density is high, twin variant one leads to the least

Figure 12: The shear stored energy quantified along the paths shown in Fig. 9(i) for grains (a) A, (b) B, (c) C and (d) D. The vertical lines indicate the experimentally observed twin nucleation sites, where the dashed lines indicate either the twin-assisted twin nucleation or ambiguous slip-assisted nucleation sites. The line colour indicates twin variant type shown in the legend.

515

516   shear stored energy compared to the other variants (and notably variant 4 and 5) and hence is

517   selected by the parent grain. Similarly for grain A, both the twins AT1 (slip assisted) and AT2

518   (twin assisted) observed experimentally correspond to variant 1 and the predictions show least

519   shear stored energy density for variant 1 at both the twin nucleation sites. This indicates that

520   the nucleation of twins assisted both by slip and twinning require least shear stored energy

521   density. Further, the shear stored energy criterion in this case is consistent with the shear strain

522   accommodation and m' analyses. For grain C, the shear stored energy correctly predicts the

523   experimentally observed active variant 4 in this grain. The distribution of stored energy density

524   in grain D led to ambiguity in predicting the twin nucleation site for twins DT1 and DT2 within

525   grain D (Fig. 9(d)(ii)). As mentioned earlier in the case of grain D, three twins DT1, DT2 and

526   DT3 of variant type 1 are experimentally observed. While the nucleation of DT3 is likely to be

527   twin-assisted, the nucleation of DT1 and DT2 are assisted by slip. DT1 has one of the twin tips

528   at the grain boundary and the other at the twin tip of DT3. From Fig. 9(d)(ii), high stored energy

529   indicates that DT1 may have nucleated at the grain boundary. However, Fig. 12(d) shows that

530   the shear stored energy for variant 1 at the grain boundary for DT1 is high. Therefore, it is

531   argued that the accumulation of high stored energy at the twin tip of DT3 due to its formation

532   may have nucleated DT1, which then propagated to the nearest grain boundary. It is shown in

533   independent studies that the formation of a twin results in high localization of stress [Kumar

534   et al. (2015)] and dislocation density [Guo et al. (2017)]. Similarly from Fig. 9(d)(ii), in the

535   case of DT2, high stored energy is observed at M and at the vicinity of N. However, the tip N

536   has the least shear stored energy for variant 1 compared to that of tip M. This implies that the

537   nucleation site of DT2 is indeed tip N instead of M (Fig. 12(d)). Further at tip N, the shear

538   stored energy of variant 1 is the least compared to the others. In addition the shear stored

539   energies for all the twin variant types at location U, which has the highest stored energy along

540   the path S1-S2 (Fig. 9(d)(i)), are high compared to those for both DT2 (tip N) and DT3. Hence

541   the absence of twin nucleation at region U for grain D results for two particular reasons. First,

542   the shear energy required for any twin variant in this region is very high compared with that at

543   observed twins DT2 and DT3. Second, the high stored energies and low shear energies

544   associated with twins DT2 and DT3 lead to early preferential nucleation of these twins, which

545   as a consequence dissipates energy, reducing the driving force for twin nucleation at region U.

546   Therefore, this detailed analysis implies that the stored energy density in conjunction with the

547   shear stored energy density appear to satisfactorily predict twin nucleation and variant

548   selection. A grain boundary location giving rise to high stored energy and low shear stored

549   energy is the most favourable for a twin nucleation site, where the twin variant selected is that

550   requiring the least shear energy.

551   **4. Discussion**

552   In the current study extruded Mg alloy WE43 (Fig. 1(a)) is compressed until ~5% strain to

553   nucleate extension twins with low/negative global Schmid factors. The CPFE calculations of

554   the resolved shear stresses determined by the local stress states are negative for all twin variants

555   (Fig. 7), which implies that these twins are not stress driven. The effective plastic strain shows

556   hotspots in the microstructure, but this distribution does not precisely predict the twin

557   nucleation sites. Therefore stored energy density, based on the evolution of local dislocation

558   structures, has been used to investigate twin nucleation. Fig. 9 shows that the locations of high

559   stored energy correspond to experimental twin nucleation sites in grains A-D. The stored

560   energy approach of twin nucleation is similar to other independent studies based on

561   heterogeneous twin nucleation theory [Capolungo and Beyerlein (2008), Beyerlein and Tomé

562   (2010), Ghazisaeidi and Curtin (2013)], according to which a twin nucleates from the existing

563   defects in the microstructure.

564   Independent experimental observations show that twins typically nucleate at low strain levels

565   for which the formation of dislocation structures (and correspondingly stored energy) is likely

566   to be limited, and for these cases, it is argued that the resolved shear stress (RSS) dominates

567   the total stored energy (i.e. not the shear energy density determining variant selection)

568   introduced above such that a simple RSS criterion is sufficient to explain twin nucleation (e.g.

569   [Liu et al. (2017), Paramatmuni and Kanjarla (2019)]). However, in contrast, nucleation of

570 twins with negative Schmid factors at lower strains that are insensitive to grain orientations

571 have also been observed [Livescu et al. (2019)]. While variant selection was not addressed in

572 [Livescu et al. (2019)], it was suggested that the nucleation of such twins may have been caused

573 by fluctuations in local stress states. Similarly, independent experimental studies have reported

574 such microstructure insensitive twins may nucleate to maintain the compatibility, orientation

575 and strain gradients in the microstructure [McClelland et al. (2015), Molodov et al. (2016)]. In

576 the present study, which examines twins of just this kind, it has been shown that such twins are

577 not in fact nucleated by local stress states, but rather, by the stored energy density.

578 Variant selection was then investigated. It is shown that shear strain accommodation and the

579 geometric compatibility factor explain the observed variant selection in grain A only.

580 Therefore, a new shear energy-based criterion has been introduced, to study variant selection.

581 It is accepted that high stress concentration at the grain boundaries supply the energy required

582 for the formation of twins. Further, the grain boundaries act as sources of defects (partials or

583 twinning dislocations) required for formation of twin nucleus. The shear energy based criterion

584 introduced in this study is based on local stress variations and is sensitive to such local

585 dislocation structures, which act as defect sources for twin embryo formation. The observed

586 twin variants selected within grains A-D correspond to those that require least predicted shear

587 energy density of formation. It is interesting to note that the twins that are nucleated by a twin

588 in a neighbouring grain (twin-assisted-twinning) also show least shear stored energy (grains A

589 and D). This indicates that the energy of formation for a twin embryo is minimum although it

590 is driven by the high stress concentration and defects supplied by twins in neighbouring grain.

591 In summary, it is shown that the stored energy in conjunction with the shear stored energy

592 locates twin nucleation site and further determines the twin variant type (Fig. 11).

593 Other energy-based variant selection approaches have also been developed. For instance, Wang

594 et al. (2012) used an analytical plastic strain energy based approach to predict the active twin

595   variants in the microstructure, where the strain energy depends largely on the strain in the twin

596   reference frame ($\varepsilon_{33}^{\text{twin}}$) and the mean free path of the twin ($\sqrt{L}$), given as $\left(\varepsilon_{33}^{\text{twin}}\middle/\sqrt{L}\right)$. In their

597   studies, the variant with highest absolute value of $\left(\varepsilon_{33}^{\text{twin}}\middle/\sqrt{L}\right)$ was selected in the

598   microstructure. Alternatively, if the sign of $\left(\varepsilon_{33}^{\text{twin}}\middle/\sqrt{L}\right)$ is strictly considered, then the twin

599   variant with the least value of $\left(\varepsilon_{33}^{\text{twin}}\middle/\sqrt{L}\right)$ was chosen in their studies, which implies that the

600   twin variant with the least associated plastic strain energy was selected in the microstructure.

601   The shear stored energy approach is similar but more robust as it is based on the local stress

602   fluctuations and dislocation structures. Further, an advantage is its implementation in full field

603   approaches such as CPFE that includes the influence of neighbouring grains, evolving local

604   dislocation structures and the strain field.

605   The stored energy density has been investigated to understand the absence of twins in the

606   apparently most favourable grain P. Here, it was found that the rate of stored energy density

607   accumulation was lowest for grain P, such that the critical energy required for twin nucleation

608   was achieved earlier in other grains. The nucleation of twins in grains A-D in principle dissipate

609   energy, redistribute stress, and correspondingly local stored energy such that the critical value

610   required for twin nucleation does not develop in grain P. The *critical* stored energy for twin

611   nucleation in this material is estimated to be 0.015 Jm^{-2}. The independent molecular dynamics

612   and DFT studies have reported that the formation energy of twin boundaries decreases with

613   increasing twin thickness, where a stable 9 layers thick twin embryo has a formation energy of

614   ~0.256 J/m^{-2} (16 meV/A^{-2}) [Wang et al. (2009a)]. Assuming that this is the energy required for

615   the formation of a twin embryo, the energy reported in the current study is about an order of

616   magnitude less. This could be due to the length-scale and continuum approximation of the

617   current CPFE approach. Further due to the weak texture, majority of the applied strain is

618　accommodated by crystallographic slip in this material. The accumulation of these dislocations

619　at the grain boundaries leads to stress concentration and act also as defect sources necessary

620　for twin embryo formation. Therefore the energy and source barriers for the formation of twins

621　is minimum, which is argued here to result in low *critical* stored energy for twin nucleation

622　compared to MD studies [Wang et al. (2009a)]. Further, while the MD studies (e.g. [Wang

623　et al. (2009a)]) provide complete localized understanding of twin formation, they do not

624　consider the effect of existing defects, alloying elements and suffers from the limitations of

625　computational cell size (not enough neighbouring grains). In addition, it appears that the MD

626　studies in [Wang et al. (2009a)] are within the bulk of pure Mg away from the grain boundary.

627　This is crucial as the high stress concentrations at the grain boundary may aid in overcoming

628　the energy barriers and reduce the total energy associated with the twin embryo, which in turn

629　reduces the energy of formation of twins.

5. Conclusions

631　• The experimental observations of compressed Mg alloy WE43 show the nucleation of

632　　extension twins with low/negative global Schmid factors within unfavourable parent

633　　grain orientations.

634　• The finite element based crystal plasticity analysis shows that the local resolved shear

635　　stresses for these twins are negative implying that they are not driven by local stress.

636　• It is shown that the stored energy density offers mechanistic insight into twin nucleation

637　　site, and acts as the driver of twin nucleation, indicating that these twins are driven

638　　predominantly by local dislocation density.

639　• Based on the investigation of accumulated stored energy density calculated at the point

640　　in the loading history when twins are first observed, a *critical* value of stored energy

641　　for twin nucleation is estimated to be 0.015 Jm^{-2}.

- Twin variant selection is explained by the shear stored energy density, where the variant selected is that which minimizes this energy density.

Therefore, the experimentally observed twin nucleation sites are identified by high stored energy density (achieving the critical value first) and the variants selected by minimising the stored shear energy which drives their formation.

References

[Al-Samman and Li (2011)]   Al-Samman, T., Li, X., 2011. Sheet texture modification in magnesium-based alloys by selective rare earth alloying. Materials Science and Engineering: A 528 (10-11), 3809–3822.

[Beyerlein et al. (2010)] Beyerlein, I., Capolungo, L., Marshall, P., McCabe, R., Tomé, C., 2010. Statistical analyses of deformation twinning in magnesium. Philosophical Magazine 90 (16), 2161– 2190.

[Beyerlein et al. (2011)] Beyerlein, I., McCabe, R., Tomé, C., 2011. Effect of microstructure on the nucleation of deformation twins in polycrystalline high-purity magnesium: A multi-scale modeling study. Journal of the Mechanics and Physics of Solids 59 (5), 988 – 1003.

[Beyerlein and Tomé (2010)]   Beyerlein, I., Tomé, C., 2010. A probabilistic twin nucleation model for hcp polycrystalline metals. Proceedings of the Royal Society A: Mathematical, Physical and Engineering Sciences 466 (2121), 2517–2544.

[Bhattacharyya et al. (2016)]   Bhattacharyya, J., Wang, F., Wu, P., Whittington, W., El Kadiri, H., Agnew, S., 2016. Demonstration of alloying, thermal activation, and latent hardening effects on quasi-static and dynamic polycrystal plasticity of mg alloy, we43-t5, plate. International Journal of Plasticity 81, 123–151.

[Bieler et al. (2014)]   Bieler, T., Eisenlohr, P., Zhang, C., Phukan, H., Crimp, M., 2014. Grain boundaries and interfaces in slip transfer. Current Opinion in Solid State and Materials Science 18 (4), 212–226.

[Bohlen et al. (2007)]   Bohlen, J., Nürnberg, M. R., Senn, J. W., Letzig, D., Agnew, S. R., 2007. The texture and anisotropy of magnesium–zinc–rare earth alloy sheets. Acta Materialia 55 (6), 2101–2112.

[Capolungo and Beyerlein (2008)]   Capolungo, L., Beyerlein, I., 2008. Nucleation and stability of twins in hcp metals. Physical review B 78 (2), 024117.

671   [Capolungo et al. (2009)]   Capolungo, L., Marshall, P., McCabe, R., Beyerlein, I., Tomé, C.,
672   2009. Nucleation and growth of twins in zr: a statistical study. Acta Materialia 57 (20), 6047 – 6056.

673   [Chen et al. (2017)]   Chen, B., Jiang, J., Dunne, F. P., 2017. Microstructurally-sensitive fatigue
674   crack nucleation in ni-based single and oligo crystals. Journal of the Mechanics and Physics of Solids
675   106, 15–33.

676   [Chen et al. (2018)]   Chen, B., Jiang, J., Dunne, F. P., 2018. Is stored energy density the primary
677   meso-scale mechanistic driver for fatigue crack nucleation? International Journal of Plasticity 101, 213–
678   229.

679   [Cheng and Ghosh (2015)]   Cheng, J., Ghosh, S., 2015. A crystal plasticity fe model for
680   deformation with twin nucleation in magnesium alloys. International Journal of Plasticity 67, 148–170.

681   [Cheng and Ghosh (2017)]   Cheng, J., Ghosh, S., 2017. Crystal plasticity finite element modeling
682   of discrete twin evolution in polycrystalline magnesium. Journal of the Mechanics and Physics of Solids
683   99, 512–538.

684   [Christian and Mahajan (1995)] Christian, J. W., Mahajan, S., 1995. Deformation twinning. Progress
685   in materials science 39 (1-2), 1–157.

686   [Dunne et al. (2012)]   Dunne, F., Kiwanuka, R., Wilkinson, A., 2012. Crystal plasticity analysis of
687   micro-deformation, lattice rotation and geometrically necessary dislocation density. In: Proc. R. Soc.
688   A. Vol. 468. The Royal Society, pp. 2509–2531.

689   [Dunne et al. (2007)]   Dunne, F., Rugg, D., Walker, A., 2007. Lengthscale-dependent, elastically
690   anisotropic, physically-based hcp crystal plasticity: application to cold-dwell fatigue in ti alloys.
691   International Journal of Plasticity 23 (6), 1061–1083.

692   [El Kadiri et al. (2015)] El Kadiri, H., Barrett, C. D., Wang, J., Tomé, C. N., 2015. Why are {101 2}
693   twins profuse in magnesium? Acta Materialia 85, 354–361.

694   [Ghazisaeidi and Curtin (2013)] Ghazisaeidi, M., Curtin, W., 2013. Analysis of dissociation of< c>
695   and< c+ a> dislocations to nucleate twins in mg. Modelling and Simulation in Materials Science and
696   Engineering 21 (5), 055007.

697   [Guan et al. (2017a)]   Guan, D., Rainforth, W. M., Gao, J., Sharp, J., Wynne, B., Ma, L., 2017.
698   Individual effect of recrystallisation nucleation sites on texture weakening in a magnesium alloy: Part
699   1-double twins. Acta Materialia 135, 14–24.

700   [Guan et al. (2017b)]   Guan, D., Rainforth, W. M., Ma, L., Wynne, B., Gao, J., 2017. Twin
701   recrystallization mechanisms and exceptional contribution to texture evolution during annealing in a
702   magnesium alloy. Acta Materialia 126, 132–144.

703 [Guan et al. (2019)]   Guan, D., Wynne, B., Gao, J., Huang, Y., Rainforth, W. M., 2019. Basal slip
704 mediated tension twin variant selection in magnesium we43 alloy. Acta Materialia 170, 1–14.

705 [Guo et al. (2014)]   Guo, C., Xin, R., Ding, C., Song, B., Liu, Q., 2014. Understanding of variant
706 selection and twin patterns in compressed mg alloy sheets via combined analysis of schmid factor and
707 strain compatibility factor. Materials Science and Engineering: A 609, 92–101.

708 [Guo et al. (2017)]   Guo, Y., Abdolvand, H., Britton, T., Wilkinson, A., 2017. Growth of {} *twins*
709 *in titanium*: *A combined experimental and modelling investigation of the local state of deformation.*
710 *Acta Materialia* 126, 221–235.

711 [Guo et al. (2015)]   Guo, Y., Collins, D., Tarleton, E., Hofmann, F., Tischler, J., Liu, W., Xu, R.,
712 Wilkinson, A., Britton, T., 2015. Measurements of stress fields near a grain boundary: Exploring
713 blocked arrays of dislocations in 3d. Acta Materialia 96, 229–236.

714 [Hadorn et al. (2013)]   Hadorn, J. P., Mulay, R. P., Hantzsche, K., Yi, S., Bohlen, J., Letzig, D.,
715 Agnew, S. R., 2013. Texture weakening effects in ce-containing mg alloys. Metallurgical and Materials
716 Transactions A 44 (3), 1566–1576.

717 [Hantzsche et al. (2010)]   Hantzsche, K., Bohlen, J., Wendt, J., Kainer, K., Yi, S., Letzig, D.,
718 2010. Effect of rare earth additions on microstructure and texture development of magnesium alloy
719 sheets. Scripta Materialia 63 (7), 725–730.

720 [Imandoust et al. (2017)]   Imandoust, A., Barrett, C., Al-Samman, T., Inal, K., El Kadiri, H.,
721 2017. A review on the effect of rare-earth elements on texture evolution during processing of
722 magnesium alloys. Journal of materials science 52 (1), 1–29.

723 [Jeong et al. (2018)]   Jeong, J., Alfreider, M., Konetschnik, R., Kiener, D., Oh, S. H., 2018. In-situ
724 tem observation of $\{101\ 2\}$ twin-dominated deformation of mg pillars: Twinning mechanism, size
725 effects and rate dependency. Acta Materialia 158, 407–421.

726 [Jiang et al. (2008)]   Jiang, J., Godfrey, A., Liu, W., Liu, Q., 2008. Identification and analysis of
727 twinning variants during compression of a mg–al–zn alloy. Scripta Materialia 58 (2), 122–125.

728 [Jonas et al. (2011)]   Jonas, J. J., Mu, S., Al-Samman, T., Gottstein, G., Jiang, L., Martin, E., 2011.
729 The role of strain accommodation during the variant selection of primary twins in magnesium. Acta
730 Materialia 59 (5), 2046–2056.

731 [Joost and Krajewski (2017)]   Joost, W. J., Krajewski, P. E., 2017. Towards magnesium alloys for
732 high-volume automotive applications. Scripta Materialia 128 (Supplement C), 107 – 112.

733 [Khosravani et al. (2015)]   Khosravani, A., Fullwood, D., Adams, B., Rampton, T., Miles, M.,
734 Mishra, R., 2015. Nucleation and propagation of twins in az31 magnesium alloy. Acta Materialia 100,
735 202–214.

736 [Kumar et al. (2016)]   Kumar, M. A., Beyerlein, I. J., McCabe, R. J., Tome, C. N., 2016. Grain
737 neighbour effects on twin transmission in hexagonal close-packed materials. Nature communications
738 7.

739 [Kumar et al. (2015)]   Kumar, M. A., Kanjarla, A., Niezgoda, S., Lebensohn, R., Tomé, C., 2015.
740 Numerical study of the stress state of a deformation twin in magnesium. Acta Materialia 84, 349–358.

741 [Kwak et al. (2016)]   Kwak, H., Xiao, J., Chaudhuri, S., 2016. Atoms-to-grains corrosion modeling
742 for magnesium alloys. In: Essential Readings in Magnesium Technology. Springer, pp. 473–477.

743 [Lim and Raj (1985)]   Lim, L., Raj, R., 1985. The role of residual dislocation arrays in slip induced
744 cavitation, migration and dynamic recrystallization at grain boundaries. Acta Metallurgica 33 (12),
745 2205–2214.

746 [Liu et al. (2018)]   Liu, C., Shanthraj, P., Diehl, M., Roters, F., Dong, S., Dong, J., Ding, W.,
747 Raabe, D., 2018. An integrated crystal plasticity–phase field model for spatially resolved twin
748 nucleation, propagation, and growth in hexagonal materials. International Journal of Plasticity 106,
749 203–227.

750 [Liu et al. (2016)]   Liu, G., Xin, R., Shu, X., Wang, C., Liu, Q., 2016. The mechanism of twinning
751 activation and variant selection in magnesium alloys dominated by slip deformation. Journal of Alloys
752 and Compounds 687, 352–359.

753 [Liu et al. (2017)]   Liu, Y., Li, N., Kumar, M. A., Pathak, S., Wang, J., Mccabe, R. J., Mara, N. A.,
754 Tome, C. N., 2017. Experimentally quantifying critical stresses associated with basal slip and twinning
755 in magnesium using micropillars. Acta Materialia 135, 411–421.

756 [Livescu et al. (2019)] Livescu, V., Beyerlein, I. J., Bronkhorst, C. A., Dippo, O. F., Ndefru, B. G.,
757 Capolungo, L., Mourad, H. M., 2019. Microstructure insensitive twinning: A statistical analysis of
758 incipient twins in high-purity titanium. Materialia 6, 100303.

759 [Livingston and Chalmers (1957)]   Livingston, J., Chalmers, B., 1957. Multiple slip in bicrystal
760 deformation. Acta Metallurgica 5 (6), 322–327.

761 [Luster and Morris (1995)]   Luster, J., Morris, M., 1995. Compatibility of deformation in two-
762 phase ti-al alloys: Dependence on microstructure and orientation relationships. Metallurgical and
763 Materials Transactions A 26 (7), 1745–1756.

764 [Mackenzie and Pekguleryuz (2008)]   Mackenzie, L., Pekguleryuz, M., 2008. The recrystallization
765 and texture of magnesium–zinc–cerium alloys. Scripta Materialia 59 (6), 665–668.

766 [McClelland et al. (2015)]   McClelland, Z., Li, B., Horstemeyer, S., Brauer, S., Adedoyin, A.,
767 Hector Jr, L., Horstemeyer, M., 2015. Geometrically necessary twins in bending of a magnesium alloy.
768 Materials Science and Engineering: A 645, 298–305.

769 [Mendelson (1969)]   Mendelson, S., 1969. Zonal dislocations and twin lamellae in hcp metals.
770 Materials Science and Engineering 4 (4), 231–242.

771 [Molodov et al. (2016)] Molodov, K. D., Al-Samman, T., Molodov, D. A., Gottstein, G., 2016. On the
772 role of anomalous twinning in the plasticity of magnesium. Acta Materialia 103, 711–723.

773 [Nabarro (1952)]   Nabarro, F. R. N., 1952. Mathematical theory of stationary dislocations.
774 Advances in Physics 1 (3), 269–394.

775 [Nervo et al. (2016)]   Nervo, L., King, A., Fitzner, A., Ludwig, W., Preuss, M., 2016. A study of
776 deformation twinning in a titanium alloy by x-ray diffraction contrast tomography. Acta Materialia 105,
777 417–428.

778 [Niewczas (2010)]   Niewczas, M., 2010. Lattice correspondence during twinning in hexagonal
779 close-packed crystals. Acta Materialia 58 (17), 5848–5857.

780 [Paramatmuni and Kanjarla (2019)]   Paramatmuni, C., Kanjarla, A. K., 2019. A crystal plasticity
781 fft based study of deformation twinning, anisotropy and micromechanics in hcp materials: Application
782 to az31 alloy. International Journal of Plasticity 113, 269 – 290.

783 [Partridge (1967)]   Partridge, P. G., 1967. The crystallography and deformation modes of
784 hexagonal close-packed metals. Metallurgical reviews 12 (1), 169–194.

785 [Pei et al. (2012)]   Pei, Y., Godfrey, A., Jiang, J., Zhang, Y., Liu, W., Liu, Q., 2012. Extension
786 twin variant selection during uniaxial compression of a magnesium alloy. Materials Science and
787 Engineering: A 550, 138–145.

788 [Proust et al. (2009)]   Proust, G., Tomé, C. N., Jain, A., Agnew, S. R., 2009. Modeling the effect of
789 twinning and detwinning during strain-path changes of magnesium alloy az31. International Journal of
790 Plasticity 25 (5), 861–880.

791 [Sevillano (2008)]   Sevillano, J. G., 2008. Geometrically necessary twins and their associated size
792 effects. Scripta Materialia 59 (2), 135–138.

793 [Styczynski et al. (2004)]   Styczynski, A., Hartig, C., Bohlen, J., Letzig, D., 2004. Cold rolling
794 textures in az31 wrought magnesium alloy. Scripta Materialia 50 (7), 943–947.

795 [Tromans (2011)]   Tromans, D., 2011. Elastic anisotropy of hcp metal crystals and polycrystals.
796 Int. J. Res. Rev. Appl. Sci 6 (4), 462–483.

797 [Wan et al. (2014)]   Wan, V., MacLachlan, D., Dunne, F., 2014. A stored energy criterion for
798 fatigue crack nucleation in polycrystals. International Journal of Fatigue 68, 90–102.

799 [Wang et al. (2014)]   Wang, F., Sandlöbes, S., Diehl, M., Sharma, L., Roters, F., Raabe, D., 2014.
800 In situ observation of collective grain-scale mechanics in mg and mg–rare earth alloys. Acta Materialia
801 80, 77–93.

802 [Wang et al. (2013)]   Wang, H., Wu, P., Wang, J., Tomé, C., 2013. A crystal plasticity model for
803 hexagonal close packed (hcp) crystals including twinning and de-twinning mechanisms. International
804 Journal of Plasticity 49, 36–52.

805 [Wang et al. (2009a)]   Wang, J., Hirth, J., Tomé, C., 2009. (1 012) twinning nucleation mechanisms
806 in hexagonal-close-packed crystals. Acta Materialia 57 (18), 5521–5530.

807 [Wang et al. (2009b)]   Wang, J., Hoagland, R., Hirth, J., Capolungo, L., Beyerlein, I., Tomé, C., 2009.
808 Nucleation of a twin in hexagonal close-packed crystals. Scripta Materialia 61 (9), 903–906.

809 [Wang et al. (2010)]   Wang, L., Eisenlohr, P., Yang, Y., Bieler, T., Crimp, M., 2010. Nucleation of
810 paired twins at grain boundaries in titanium. Scripta Materialia 63 (8), 827–830.

811 [Wang et al. (2012)]   Wang, S., Schuman, C., Bao, L., Lecomte, J., Zhang, Y., Raulot, J., Philippe,
812 M., Zhao, X., Esling, C., 2012. Variant selection criterion for twin variants in titanium alloys deformed
813 by rolling. Acta Materialia 60 (9), 3912–3919.

814 [Wilson et al. (2019)]   Wilson, D., Wan, W., Dunne, F. P., 2019. Microstructurally-sensitive fatigue
815 crack growth in hcp, bcc and fcc polycrystals. Journal of the Mechanics and Physics of Solids 126, 204–
816 225.

817 [Wu et al. (2015)]   Wu, P., Guo, X., Qiao, H., Lloyd, D., 2015. A constitutive model of twin
818 nucleation, propagation and growth in magnesium crystals. Materials Science and Engineering: A 625,
819 140–145.

820 [Xin et al. (2015)]   Xin, R., Liang, Y., Ding, C., Guo, C., Wang, B., Liu, Q., 2015. Geometrical
821 compatibility factor analysis of paired extension twins in extruded mg–3al–1zn alloys. Materials &
822 Design 86, 656–663.

823 [Zeghadi et al. (2007)] Zeghadi, A., Forest, S., Gourgues, A.-F., Bouaziz, O., 2007. Ensemble
824 averaging stress–strain fields in polycrystalline aggregates with a constrained surface microstructure–
825 part 2: Crystal plasticity. Philosophical Magazine 87 (8-9), 1425–1446.

826 [Zhang et al. (2011)]   Zhang, P., Balint, D., Lin, J., 2011. Controlled poisson voronoi tessellation for
827 virtual grain structure generation: a statistical evaluation. Philosophical Magazine 91 (36), 4555–4573.

828 [Zhang et al. (2018)]   Zhang, Z., Lunt, D., Abdolvand, H., Wilkinson, A. J., Preuss, M., Dunne, F. P.,
829 2018. Quantitative investigation of micro slip and localization in polycrystalline materials under
830 uniaxial tension. International Journal of Plasticity.

831 [Zheng et al. (2019)]   Zheng, Z., Prastiti, N. G., Balint, D. S., Dunne, F. P., 2019. The dislocation
832 configurational energy density in discrete dislocation plasticity. Journal of the Mechanics and Physics
833 of Solids 129, 39–60.

834 [Zhou et al. (2020)]   Zhou, B., Wang, L., Jin, P., Jia, H., Roven, H. J., Zeng, X., Li, Y., 2020.
835 Revealing slip-induced extension twinning behaviors dominated by micro deformation in a magnesium
836 alloy. International Journal of Plasticity, 102669.

837